BRILLOUIN LIGHT SCATTERING FROM CARBON NANOTUBE ARRAYS

ANNA MARIA POLOMSKA

BRILLOUIN LIGHT SCATTERING FROM CARBON NANOTUBE ARRAYS

by

Anna Maria Polomska

A Thesis Submitted in Partial Fulfilment of
the Requirements for the Degree of

Master of Science

Department of Physics and Physical Oceanography
Memorial University of Newfoundland

August, 2005

St. John's Newfoundland

Library and
Archives Canada

Published Heritage
Branch

395 Wellington Street
Ottawa ON K1A 0N4
Canada

Bibliothèque et
Archives Canada

Direction du
Patrimoine de l'édition

395, rue Wellington
Ottawa ON K1A 0N4
Canada

Your file Votre référence
ISBN: 978-0-494-19416-4
Our file Notre référence
ISBN: 978-0-494-19416-4

NOTICE:
The author has granted a non-exclusive license allowing Library and Archives Canada to reproduce, publish, archive, preserve, conserve, communicate to the public by telecommunication or on the Internet, loan, distribute and sell theses worldwide, for commercial or non-commercial purposes, in microform, paper, electronic and/or any other formats.

The author retains copyright ownership and moral rights in this thesis. Neither the thesis nor substantial extracts from it may be printed or otherwise reproduced without the author's permission.

AVIS:
L'auteur a accordé une licence non exclusive permettant à la Bibliothèque et Archives Canada de reproduire, publier, archiver, sauvegarder, conserver, transmettre au public par télécommunication ou par l'Internet, prêter, distribuer et vendre des thèses partout dans le monde, à des fins commerciales ou autres, sur support microforme, papier, électronique et/ou autres formats.

L'auteur conserve la propriété du droit d'auteur et des droits moraux qui protège cette thèse. Ni la thèse ni des extraits substantiels de celle-ci ne doivent être imprimés ou autrement reproduits sans son autorisation.

In compliance with the Canadian Privacy Act some supporting forms may have been removed from this thesis.

While these forms may be included in the document page count, their removal does not represent any loss of content from the thesis.

Conformément à la loi canadienne sur la protection de la vie privée, quelques formulaires secondaires ont été enlevés de cette thèse.

Bien que ces formulaires aient inclus dans la pagination, il n'y aura aucun contenu manquant.

Canada

Abstract

Brillouin light scattering spectroscopy was used to investigate the vibrations in two carbon nanotube arrays (one with 200 nm – 300 nm of the nanotubes protruding above the alumina substrate surface and one with the top of nanotubes flush with the alumina surface) and two alumina templates with holes (non-annealed and annealed). The carbon nanotube array with nanotubes protruding above the surface was exposed to vacuum and various gases (H_2, CH_4, Ar, Kr, CF_4, SF_6, C_2F_6 and air). For this sample at least three Brillouin peaks were observed for free spectral range up to 50 GHz. The Brillouin modes were at the frequency shifts of ~ 1.3 GHz, ~ 5 GHz and ~ 7 GHz. None of the modes exhibited surface character. One additional peak of Gaussian profile and zero frequency shift, originating from the gas surrounding the sample was also noticed. The line shapes and intensities of the peaks depended on the gaseous environment to which the sample was exposed. The most significant changes in intensity and frequency shifts were observed when H_2 was used as an environment. Brillouin scattering experiments performed on the sample of carbon nanotube array with zero exposed length and on non-annealed and annealed alumina templates that represent intermediate steps in the fabrication of carbon nanotube arrays aided in the determination of the character and origin of the peaks observed in the carbon nanotube array spectra. The values of phonon velocities were determined using a coarse approximation. It is possible that these peaks originate due to the bulk modes propagating in the array. In this case the phonon velocities were estimated to be a few hundreds meters per second for the peak at $\sim 1.3\ GHz$ and between $1000-2000\ m/s$ for peaks at 5 and 7 GHz, depending on the gas surrounding the sample. It is also conceivable that the peaks are transverse, longitudinal and/or twist (torsional) modes that propagate in individual tubes.

Acknowledgments

I would like to thank my supervisor Dr. Todd Andrews for all the help, suggestions and direction that he provided during two years of work on this project.

I also would like to thank to Dr. Maynard Clouter for constructing the sampler holder and letting us use it as much as we needed it.

I know I have many fellow students to thank. Among all of them, hoping I would not offend anybody, two of them could and should be distinguished as “primi inter pares”. Marek Bromberek, mainly for his finite though extremely large patience and unbelievable resourcefulness and Chris Young for building the gas holding system, making fun of my slow pace in writing, and inspiring discussions about significant, more or less work related problems. I also would like to say thank you to Bert Boyd for all the support he provided while I was writing this thesis. In addition to that I would like to thank all my office mates (both temporary and permanent ones) who helped in creating a supportive and friendly environment.

This part is going to be slightly more personal and maybe a little sappy but I also would like to attach less official but equally important "Thank you" to all the people who contributed to this thesis not through their knowledge about Physics but by being who they are and giving me all they could. First of all my Mom who always encouraged me to look for my place in the world no matter what obstacles happen. Along with that - my Dad, who challenged and even from distance challenges me every day building up my life endurance and strength. If it was not for them I probably would have never taken a chance I had. Secondly to my Grandmothers who knew how to ask for and pass spiritual help.

Podziękowania

Ta część będzie nieco bardziej osobista i może trochę sentymentalna, ale chciałabym dołączyć mniej oficjalne, ale równie ważne "Dziękuję" każdemu, kto przyczyniłsię do powstania tej pracy nie dzięki swej wiedzy o fizyce, ale przez bycie kim jest i dając wszystko, co mógł. Przede wszystkim mojej Mamie, która zawsze zachęcała mnie do szukania swojego miejsca w świecie bez względu na to, jakie przeszkody napotkam. Równie mocno Tacie, który stawiał, i nawet teraz, z daleka, stawia wyzwania budując moją wytrzymałość i siłę. Gdyby nie oni, prawdopodobnie nigdy nie skorzystałabym z szansy, którą miałam. Chciałabym również podziękować moim Babciom, które wiedzą jak otrzymać i przekazać duchową pomoc.

Contents

List of Tables

List of Figures

List of Symbols

$\mathbf{a_1}$, $\mathbf{a_2}$ - unit lattice vectors of carbon nanotube

c - speed of light

$\mathbf{C_h}$ - chiral vector

d - distance between mirrors

$\Delta\lambda$ - spectral interval around a wavelength

$\Delta\nu$ - full width in half maximum

ϵ - dielectric constant

f - focal length

$f_{\#}$ - f-number

F - finesse

h - Planck constant

η - real part of refractive index

k_B - Boltzmann constant

$\mathbf{k_i}$ - incident light wavevector

$\mathbf{k_s}$ - scattered light wavevector

κ - imaginary part of refractive index n

L - optical spacing

$\bar{l}$ - mean free path

λ_e - distance between planes of compression and rarefaction

λ_i - wavelength of the incident light

λ_s - wavelength of the scattered light

m - molecular mass

n - refractive index of the medium

ν_i - incident light frequency

ν_s - scattered light frequency

ν - phonon frequency

$\mathbf{q}$ - phonon wavevector

θ - angle between incident and scattered light

θ_i - angle of incidence

θ_s - scattering angle

R^2 - correlation coefficient

T - absolute temperature

v - phonon velocity

x - distance between nanotubes in array

y - outer diameter of the nanotube

List of Abbreviations

BS - beam splitter

$CNT - 0$ - carbon nanotube array with nanotubes flush with the alumina surface

$CNT - 2$ - carbon nanotube array with nanotubes protruding above the surface

FPI - Fabry-Perot interferometer

$FWHM$ - full width at half maximum

HWP - half-wave plate

M - mirror

$T - 519$ - alumina template with holes arranged in close-packed hexagonal array

$T - 519a$ - alumina template with holes arranged in close-packed hexagonal array, annealed

V - valve

$VNDF$ - variable neutral density filter

Chapter 1

Introduction

1.1 Carbon Nanotubes

A carbon nanotube can be imagined as a graphite sheet seamlessly rolled up into a tube or cylinder [1] with a diameter of the order of ten nanometers. The first carbon nanotubes, prepared in 1991 by Iijima [2], were grown on the negative end of a carbon electrode used in the direct current arc-discharge evaporation of carbon in a vessel filled with argon under a pressure of 13.33 kPa. The tubes produced were no longer than 1 μm, with diameters ranging from a few to a few tens of nanometers. Carbon nanotubes can be single-walled (consisting of one tube) or multi-walled (consisting of between 2 and 50 coaxial tubes).

The structural parameters of a nanotube are specified by the pair of integers (m, n) that are components of the chiral vector $\mathbf{C_h}$ along the primitive lattice vectors $\mathbf{a_1}$ and $\mathbf{a_2}$, as presented in Figure 1.1. The value of the angle θ varies between 0° and 30°.

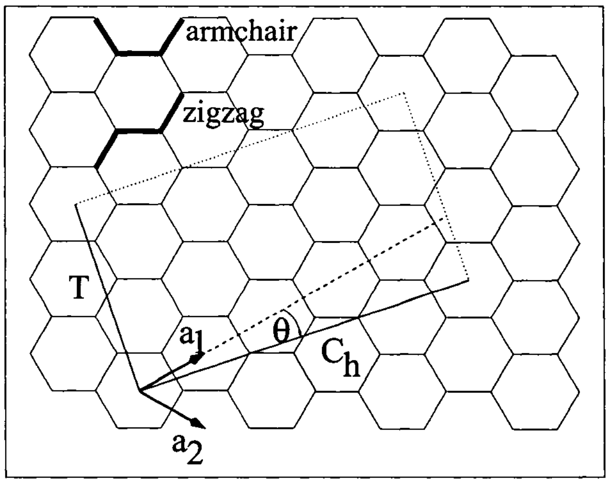

Figure 1.1: Schematic representation of construction of a nanotube. $\mathbf{a_1}$, $\mathbf{a_2}$ - unit lattice vectors of carbon nanotube, $\mathbf{C_h}$ - chiral vector, T - tube axis.

Depending on the configuration of the carbon bonds around the circumference of the tube, the carbon nanotube is either of the armchair ($\theta = 30°$, (n, n)), zigzag ($\theta = 0°$, $(n, 0)$) or chiral type, as shown in Figure 1.2. Nanotubes can be either semiconducting or metallic [3] depending on the chiral vector components. All (n, n) nanotubes are metallic, while others are semiconductors with a band gap depending on the inverse of the nanotube diameter [4]. In the example presented in Figure 1.1 the value of m is 5 and the value n is 2 the nanotube is of the chiral type.

As their physical, elastic and electronic attributes, such as nanosize, high Young's modulus [6], high conductivity that depends on microstructure, ability to support large current density without dissipation, thermal conductivity higher than that of diamond [7], [8] and sensitivity to gases [9] are both unique and interesting, carbon nanotubes became the object of detailed studies and careful examination.

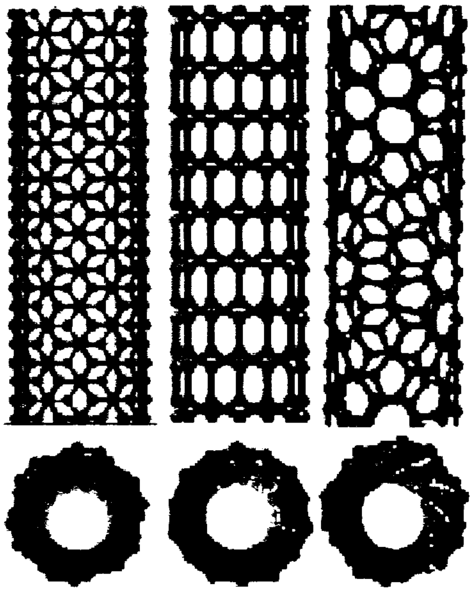

Figure 1.2: Schematic illustration of the structures of airmchair (left), zigzag (center) and chiral (right) single-walled nanotubes [5].

This was followed by propositions of various applications. Due to their electronic properties, carbon nanotubes have been used in electronic devices such as field-effect transistors [10], [11], single-electron transistors [12], electron field emitters [13], or logic circuits [14]. Carbon nanotubes have also been shown to be capable of "ingesting" bipolar molecules of a fluid surrounding the tubes [15]. The transport and electronic properties of carbon nanotubes might be impacted by the surrounding fluid via physisorption (adsorption), chemisorption or formation of thin sheets of molecules trapped within nanoscopic space [16]. This feature of nanotubes could result in their application as chemical sensors [17]. So far various authors present different concepts and arguments concerning this subject, both in discussion of the mechanism and types of gases. Some reports claim that nanotubes are extremely sensitive to O_2 [18], [19] and it is adsorbed by them [20], [21] what causes changes in electronic properties of nanotubes [22]. Exposure to N_2 and He change the resistance of the nanotubes, however these gases influence electronic properties less significantly than O_2 [22]. Other authors [9] state that O_2, N_2, water or CO_2 do not influence the material properties. Due to high and reversible hydrogen adsorption, carbon nanotubes were considered as hydrogen storage media [23], [24]. This concept, however is still the subject of active debate and research [5]. The electrochemical activity for intercalation of lithium ions [25] suggests an application in lithium-ion batteries [26].

1.2 Carbon Nanotube Arrays

The precision in determining the direction of the growth is the main challenge in the production of carbon nanotubes as elements of the devices because most of the applications will require nanotubes with uniform, well-controllable physical properties. Some electronic and photonic devices (field emission displays and data storage elements [27]) and devices used for IR imaging (focal plane arrays [28]) need well-ordered, high-density carbon nanotube arrays. Vertical nanotubes that were grown within the pores of alumina templates (carbon nanotube arrays) were found to conduct electric current and proved their usefulness as three-dimensional contacts [29].

A schematic picture of an ordered carbon nanotube array is presented in Figure 1.3. Such arrays are fabricated using three main techniques: (*i*) chemical vapor deposition of hydrocarbon gas on various substrates [30], (*ii*) plasma-enhanced chem-

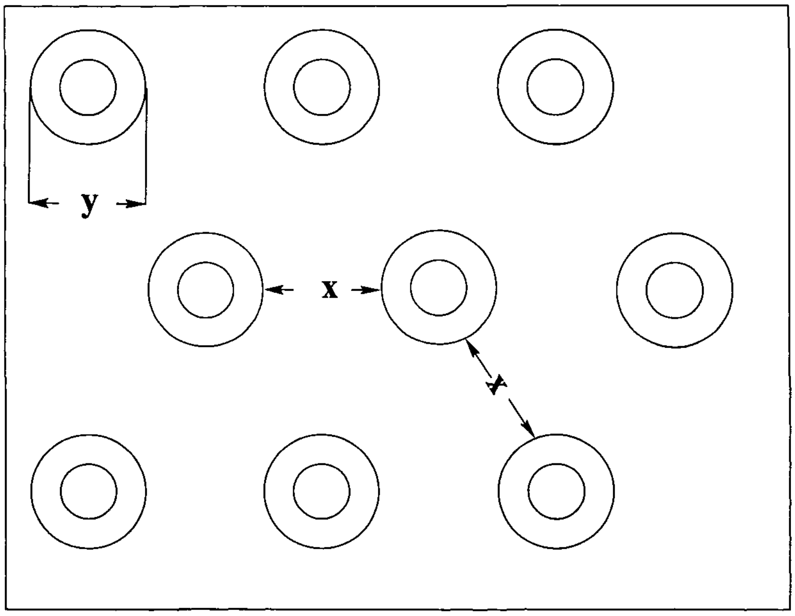

Figure 1.3: Schematic image of hexagonally ordered array of carbon nanotubes. y is the outer diameter of the multiwall nanotube, x stands for the typical distance between tubes.

ical vapor deposition on Ni dot arrays [31] and (*iii*) pyrolysis of acetylene on cobalt within a hexagonal close-packed nanochannel alumina template [32], [33].

The first method can be used for fabricating carbon nanotube arrays on bulk silica and film-like silica substrates. In the case of growth on bulk silica substrates the resulting nanotubes are aligned and approximately perpendicular to the substrate. They are multi-walled and typically consist of $\sim$ 40 tubes. The nanotubes grow at a rate of about 20 $\mu m/h$ and achieve a length of 100 μm. The value of diameter y (see Figure 1.3) is $\sim$ 30 nm and can be controlled by the catalyst used. The spacing between tubes x is 100 nm. When film-like silica is used as a substrate the nanotubes reach about 2 *mm* length. The value of y varies from 20 to 40 *nm* and is uniform within the array. The value of the spacing x is $\sim$ 100 μm.

Using the second method, plasma-enhanced chemical vapor deposition on Ni dots, closed-end, vertically aligned free standing nanotubes organized in a pattern the same as the one created by Ni dots (*e.g.,* line, array) are obtained. The diameter y at the end of the closed-end tube is about $10 - 20$ *nm*. The distance between tubes is determined by the organization of the Ni dots.

Using the third method of fabrication, pyrolysis of acetylene on cobalt within a hexagonal close-packed nanochannel alumina template, nanotube arrays grown perpendicularly to the substrate are obtained. The advantages of this method are the fact that synthesis can be scaled up with the size of the template and its low cost. Carbon nanotubes produced this way are characterized by excellent uniformity in size and have no defects over relatively long length scales [28]. The tubes are exposed by etching the alumina matrix with a mixture of chromic and phosphoric acid. The nanotubes in the array are parallel to one another, simultaneously forming a close-packed hexagonal array. All of them are open-ended, multi-walled and of comparable length and diameter. The mean outer diameter of an individual tube is $y \sim 50$ *nm*. The distance, x, between tubes is comparable to their outer diameter. The etching of the alumina at the end of the production process allows a few percent of the total length of the nanotubes to protrude above the alumina surface.

1.3 Previous Studies

The number of experiments performed using Brillouin spectroscopy to investigate carbon nanotubes is few. Brillouin light scattering was used to examine elastic properties of free standing films of single-walled carbon nanotubes [34], [35] grouped in bundles, both aligned around a magnetic field direction and randomly oriented. In the first case, a broad peak was observed at about 45 GHz, where the peak shape and position were independent of the scattering angle. The presence of this peak depended on the orientation of the sample. For the randomly oriented nanotubes, one peak at about 40 GHz was observed, whereas for the aligned nanotubes the existence of the peak and its frequency shift depended on the orientation of the sample. When the scattering plane was parallel to the nanotubes one broad peak, of which shape and position were independent of the angle of incidence was observed at around 45 GHz. When the sample was rotated by 90°, this peak disappeared. From the dispersion relation of the acoustic modes the two-dimensional Young modulus of single curved graphitic plane was estimated. The obtained value, $E_{2D} = 110\ N/m$, is of the same order of magnitude as the $C - C$ atomic force constant in a graphitic plane [36].

Young [37] used Brillouin light scattering to observe acoustic phonons in ordered carbon nanotube arrays in various gaseous environments. The main focus of his work were very low frequency modes of carbon nanotubes surrounded by a number of gases of different polarizability and mass. In the low frequency range two peaks were observed, one at $\sim 0.7\ GHz$ and one at $\sim 1.3\ GHz$. The intensity ratio of these peaks, the object of main interest, showed linear dependence on the density (molecular mass) of the gas used in the experiment.

Brillouin light scattering experiments from materials related to carbon nanotube arrays - C_{70} and C_{60} thin films [38] - show modes due to Rayleigh surface wave at 4.8 and 4.3 GHz, respectively, as well as modes due to longitudinal bulk waves at 25 and 30 GHz, respectively. The velocities of the surface and bulk modes were determined together with bulk, shear and Young moduli and Poisson's ratios of both films. The values of bulk, shear and Young moduli of C_{70} are found to be 11.3, 3.2 and 8.7 GPa, respectively. The corresponding values for C_{60} are 14.9, 4.7 and 12.7 GPa. Poisson's ratios for both types of this films are comparable, the values are 0.37 for C_{70} and 0.36 for C_{60}.

1.4 Overview

In this thesis the Brillouin light scattering technique was used to examine four samples representing four stages in the production of ordered carbon nanotube arrays. The first of these was an ordered carbon nanotube array with $\sim 5\%$ of the total length of the nanotubes protruding above the surface of the alumina template $(CNT-2)$. Brillouin spectra at a free spectral range (FSR) from 50 to 8 GHz were collected in vacuum and various gaseous environments to investigate the effect of gas on the Brillouin spectra of carbon nanotube arrays and therefore on the elastic properties of the array. No studies were done about the influence of the gas surrounding nanotubes on their elastic properties. The presence of the gas may alter the frequencies of the vibrational modes of the nanotubes, what can be seen in the Brillouin spectra. Brillouin spectra in air and vacuum were also collected from a non-annealed alumina template with holes arranged in a hexagonal, close-packed array ($T-519$), an annealed alumina template with holes ($T-519a$) and highly-ordered carbon nanotube array with the top of the nanotubes flush with the surface of the alumina template ($CNT-0$). The latter three samples were studied to aid in the determination of the origin of the modes observed in the spectra collected from $CNT-2$.

Chapter 2

Theory

2.1 Theory of Brillouin Light Scattering

The samples studied in this work are either opaque or semi-opaque and, in some cases, were surrounded by a gas. These media scatter light by different mechanisms and therefore this chapter is divided into sectionst that trat each type of material separately.

2.1.1 Classical Theory

In the classical theory of thermal scattering at a temperature $T \geq 0K$, a medium is treated as if elastic waves of all frequencies were passing through it in all directions and its internal structure is disregarded. Each of these waves will form planes of compression (C) and rarefaction (R) that alternate as shown in Figure 2.1 and are a distance λ_e apart. The presence of these planes makes the medium optically inhomogeneous.

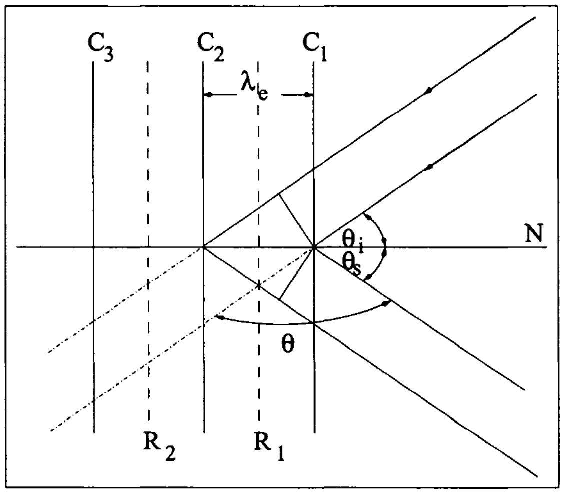

Figure 2.1: Wave picture of light scattering. C - planes of compression, R - planes of rarefaction, N - normal, θ - angle of scattering. After [39].

When a ray of incident light, characterized by wavelength λ_i and frequency ν_i, is directed so it makes an angle θ_i with the plane of compression of the sound wave propagating in the medium along an arbitrary direction, it will be reflected or scattered at the layer where the change in density and therefore in the refractive index occurs. The scattered ray makes an angle θ_s with the plane of compression. The reflections will take place on each successive plane if the Bragg relation

$$\lambda_i = 2\lambda_e \sin\frac{\theta}{2}, \tag{2.1}$$

where θ is the angle between the incident and scattered light, is satisfied. The planes C_i are moving with velocity v and therefore the reflected light is Doppler-shifted by an amount

$$\nu = \pm\frac{2\nu_i v n}{c}\sin\frac{\theta}{2}, \tag{2.2}$$

where c is the speed of light in the vacuum and n is a refractive index of the medium.

2.1.2 Quantum Theory

The energy of the acoustic waves that propagates in the medium can be quantized [40] and elastic waves in the medium can be considered as consisting of phonons. Quantum mechanically, Brillouin light scattering may be therefore described as scattering of a photon of incident light, characterized by frequency ν_i and wave vector $\mathbf{k_i}$, by a phonon of frequency ν and wave vector $\mathbf{q}$. The first order of this process can be described as creation and annihilation of phonons. This is shown schematically in the Figure 2.2.

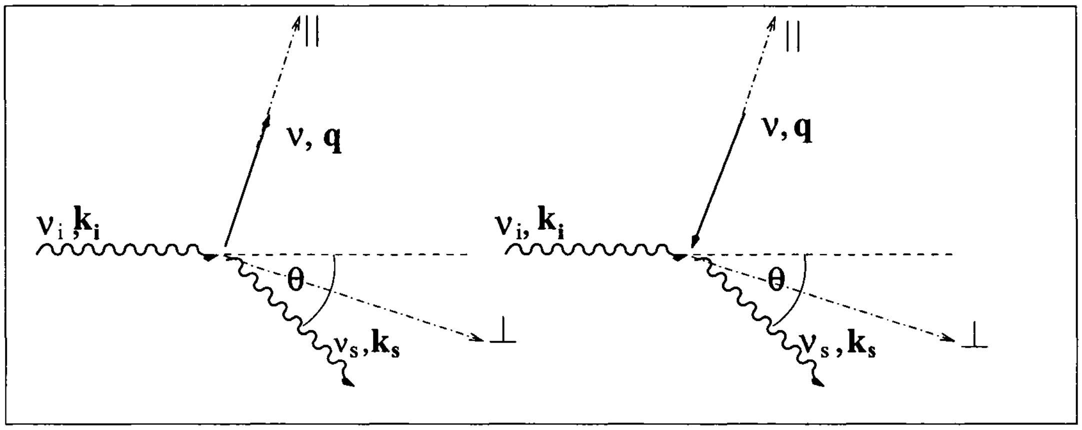

Figure 2.2: Schematic of the process of creation (Stokes region, on the left) and annihilation (anti-Stokes region, on the right) of a phonon in the process of light scattering. ν_i, $\mathbf{k_i}$ - frequency and wave vector of incident light, ν_s, $\mathbf{k_s}$ - frequency and wave vector of scattered light, ν, $\mathbf{q}$ - frequency and wave vector of the phonon.

The conservation of energy and momentum during the scattering process leads to

$$h\nu_s = h\nu_i \pm h\nu, \tag{2.3}$$

and

$$h\mathbf{k_s} = h\mathbf{k_i} \pm h\mathbf{q}, \tag{2.4}$$

where the indices i and s refer to the incident and scattered light, respectively. The scattered light therefore displays a frequency shift of

$$\nu_i - \nu_s = \nu \tag{2.5}$$

Breaking the condition (2.4) into components along the axes parallel and perpendicular to the direction of the phonon propagation as shown in the Figure 2.2, one obtains:

$$k_{s\|} = k_{i\|} \pm q_{\|}, \tag{2.6}$$

$$k_{s\perp} = k_{i\perp} \pm q_{\perp}. \tag{2.7}$$

Using the fact that $q_{\perp} = 0$ and $q_{\|} = q$, as can be seen in Figure 2.2, and the approximation $k_i \approx k_s$, justified by the fact that a Brillouin frequency shift is significantly smaller than the frequency of the incident and scattered light, one can convert Equation (2.6) into

$$k_i \sin\left(-\frac{\theta}{2}\right) = k_i \sin\left(\frac{\theta}{2}\right) \pm q. \tag{2.8}$$

Therefore the expression for the magnitude of the phonon vector takes the form:

$$q = 2k_i \sin\frac{\theta}{2}. \tag{2.9}$$

Using relations

$$\nu = \frac{vq}{2\pi} \tag{2.10}$$

and

$$\nu_i = \frac{ck_i}{2\pi} \tag{2.11}$$

the formula (2.9) can be transformed into

$$\frac{\nu}{v} = \frac{2\nu_i n}{c} \sin\frac{\theta}{2}. \tag{2.12}$$

The Brillouin shift is therefore:

$$\nu = \frac{2\nu_i n v}{c} \sin\frac{\theta}{2}, \tag{2.13}$$

which is equivalent to Equation (2.2) derived using the classical theory of scattering.

2.2 Brillouin Light Scattering in Fluids

In the case of fluids, the atoms and particles are able to move over large distances because there is no long range order. According to [41], if the condition

$$\bar{l} \ll \frac{\lambda_i}{n}, \tag{2.14}$$

is satisfied the medium can be considered continuous and is characterized by the optical dielectric constant ϵ. In the Equation 2.14, $\bar{l}$ is the mean free path of the molecules, λ_i is the wavelength of the incident light and n is the refractive index of the medium. The motions of molecules in the medium leads to the appearance of fluctuations of the density and orientation of the molecules.

At low densities the molecules of the fluids can be treated as independent scattering sources. When monochromatic light is incident on the volume, a Doppler-broadened single line with Gaussian distribution of intensity [42] is present. The full width at half maximum $(FWHM)$, $\Delta\nu$ of this line is given by:

$$\Delta\nu = 4\left(2\ln 2\frac{k_B T}{mc^2}\right)^{\frac{1}{2}} \nu_i \sin\frac{\theta}{2}, \tag{2.15}$$

where m is the molecular mass of the fluid particle, k_B is the Boltzmann constant and T is the absolute temperature of the gas.

2.3 Brillouin Light Scattering in Solids

In crystalline materials along any direction there are three kinds of elastic waves, one quasi-longitudinal and two quasi-transverse, each of different velocity v. In amorphous solids there are only two distinct values of v, as both transverse waves are degenerate.

Acoustic waves can scatter light by two mechanisms [43]: (i) the surface ripple mechanism and (ii) the bulk elasto-optic mechanism. The surface ripple mechanism by which incident light is reflected from the dynamic acoustic deformation of the sample surface and only the component of the wave vector that is parallel to the surface is conserved. The bulk elasto-optic mechanism in which the coupling of incident and scattered light occurs by acoustic modulation of the dielectric constant and in the case of transparent solids with real wave vectors all components of the wave vector are conserved. In the first approximation surface acoustic waves scatter light by the way of the first mechanism and bulk acoustic waves scatter light through the bulk elasto-optic mechanism. Bulk waves can, however, cause surface deformation and hence contribute to surface ripple scattering. In the same way, surface acoustic waves cause distortions that can penetrate into the bulk of the material by a distance comparable to the length of the acoustic wave which results in a bulk elasto-optic contribution to the surface light scattering. The main determinant of the importance of the scattering mechanisms is the opacity of the solid.

2.3.1 Brillouin Light Scattering in Transparent Materials

For transparent materials the incident light illuminates a relatively large volume of the examined material. The energy (2.3)) and momentum conservation (2.4) laws combine according to the bulk elasto-optic mechanism. The result is a spectrum with a set of sharp peaks. The elastic waves in transparent solids give rise to Brillouin scattering. The elasto-optic constants of the material determine the intensity of the scattered light. The angle of incidence θ_i and angle of scattering θ_s change according to Snell's law [44] and become

$$\sin\theta_i = n\sin\theta_i' \tag{2.16}$$

$$\sin\theta_s = n\sin\theta'_s \tag{2.17}$$

where θ'_i is an angle of incidence in the medium, θ'_s is an angle of scattering in the medium. Angles θ'_i, θ'_s and θ are related by identity

$$\theta = \pi + \theta'_i - \theta'_s. \tag{2.18}$$

Equations (2.6) and (2.7) can be written in the form

$$k_i n\sin\theta'_i + k_s n\sin\theta'_s = q_{\|} \tag{2.19}$$

$$k_i n\cos\theta'_i + k_s n\cos\theta'_s = q_{\perp}. \tag{2.20}$$

Using a first order approximation when $k_i = k_s$ leads to the following scattering condition:

$$k_i n(\sin\theta'_i + \sin\theta'_s) = q_{\|} \tag{2.21}$$

$$k_i n(\cos\theta'_i + \cos\theta'_s) = q_{\perp}. \tag{2.22}$$

The magnitude of phonon wave vector q is therefore:

$$q = k_i n\sqrt{(\sin\theta'_i + \sin\theta'_s)^2 + (\cos\theta'_i + \cos\theta'_s)^2} \tag{2.23}$$

Simlpifying Equation (2.23) using trigonometric formulas leads to

$$q = k_i n\sqrt{2(1+\cos(\theta_i - \theta_s))}. \tag{2.24}$$

Using Equations (2.18) and the half-angle formula Equation (2.24) transforms into

$$q = k_i n\cos\left(\frac{\pi}{2} - \frac{\theta}{2}\right) = k_i n\sin\frac{\theta}{2}. \tag{2.25}$$

Using Equations (2.10) and (2.11) transforms Equation (2.25) into

$$\nu = 2\frac{vn\nu_i}{c}\sin\frac{\theta}{2}. \tag{2.26}$$

which is equivalent to Equation 2.13.

2.3.2 Brillouin Light Scattering in Opaque Materials

Scattering from an opaque material is confined to a region near the surface [45], which makes the depth of scattering volume at most comparable to an acoustic wavelength [46], therefore the signal is weak in comparison to the signals obtained in Brillouin light scattering in transparent media. The presence of optical absorption has an influence on the momentum conservation rule [47]. As the opacity of the medium increases so does the imaginary part of the wave vector of the phonon [43] obtained in the Equation (2.4). It allows the creation or annihilation phonons not of one fixed wave vector $q = K'$, but within a spread of wave vectors $\Delta q \sim K''$ and therefore of frequencies [48]. Condition (2.7) breaks down due to the uncertainty principle, the wave vector component perpendicular to the surface $q_\perp$ is not conserved in the interaction between light and acoustic wave [49] and leads to a range of allowed **q** vectors. The peak position does not change and remains as given by Equation (2.13), however the peak becomes broadened with a $FWHM$ $\Delta\nu$ of

$$\Delta\nu = \frac{2}{\pi}vk_i\kappa, \tag{2.27}$$

where κ is the imaginary part of the complex refractive index n of the opaque medium [50].

For an isotropic opaque solid the Brillouin spectrum usually consists of an intense peak from inelastically scattered light that results from the Rayleigh surface acoustic wave. Additionally a much less intense "Lamb shoulder" is present that extends from threshold to higher frequencies. The "Lamb shoulder" is a result from coupling to the continuum of bulk modes through the deformation caused by them at the surface. While dealing with more complicated materials (anisotropic solids, thin supported films) a variety of excitations, depending on the experimental conditions and the nature of the sample might be found such as quasi-Rayleigh waves, Sezawa and pseudo-Sezawa modes, Lamb waves, various pseudo-surface acoustic waves and interface excitations [51].

2.3.3 Surface Brillouin Light Scattering

The geometry of the surface Brillouin light scattering is presented in Figure 2.3. For scattering from surface phonons, condition (2.7) breaks down due to the fact that the perpendicular component of phonon amplitude $q_\perp$ decreases to zero [47] at the depth of a few surface acoustic wavelengths.

The surface wavevector $\mathbf{q} = q_{||}$ is defined through Equation (2.6) and leads to a peak in the scattered light at a frequency shift given by Equation (2.10), with v standing for the surface phonon velocity. The frequencies of surface waves are smaller

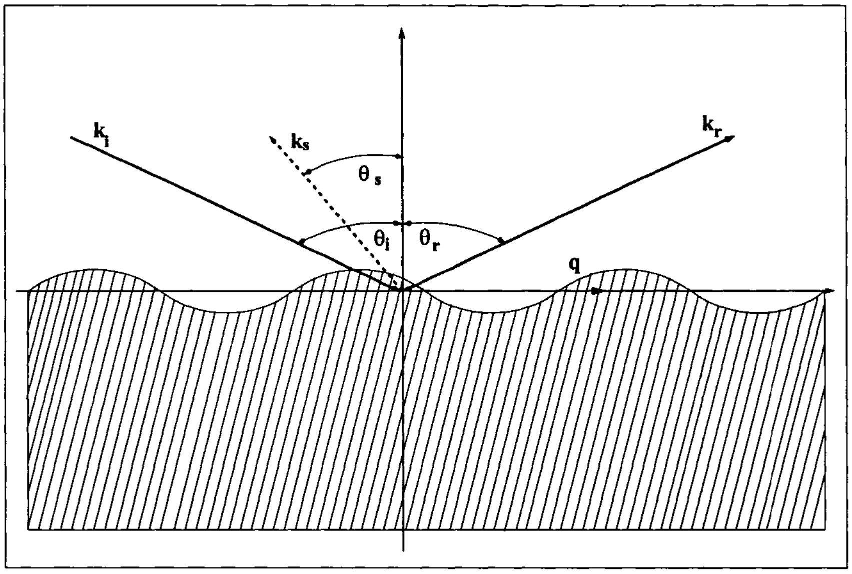

Figure 2.3: Schematic of the surface scattering geometry showing incident and scattered light wave vectors $\mathbf{k}_i$ and $\mathbf{k}_s$ and the surface phonon vector $\mathbf{q}$. After [43].

than that frequencies of the bulk acoustic phonons of the same wavevector. The frequency shift for the surface mode is a function of the angle of incidence and is equal to [52]:

$$\nu = \frac{2v}{\lambda_i} \sin\theta_i. \tag{2.28}$$

Chapter 3

Methods and Materials

3.1 Experimental Setup

Figure 3.1 schematically shows the experimental setup. The source of light is a Coherent $Verdi-V2$ diode pumped $Nd:YVO_4$ laser operating on second harmonic and producing a vertically polarized beam of light at a wavelength of $\lambda = 532\ nm$. The output power of the laser is 2 W and the current is in the range of $16-17\ A$. The power of the light is reduced by a variable neutral density filter $VNDF_1$ and its plane of polarization is rotated by 90° by the half wave plate HWP. The horizontally polarized beam is incident on a beam splitter BS, where a small fraction of its power is reflected, the rest is transmitted. The light reflected from the beam splitter acts as a reference beam and is directed to the tandem Fabry-Perot interferometer by the mirror M_2. The intensity of the reference beam is controlled by the variable neutral density filter $VNDF_3$. The reference beam is used to maintain mirror alignment for both Fabry-Perot interferometers. A second function of the reference beam is to prevent saturation of the detector when scanning over the region of intense, elastically scattered light.

The light transmitted through the BS is incident on mirror M_1 which changes the direction of the beam by 90°. The light passes through a set of filters F that decrease the beam power to the desired value, and an aperture A. The beam then undergoes total internal reflection in the prism P and is focused on the sample S by a lens f with a focal length of 5 cm and an $f/\#$ of 2.8. The scattered light is collected by the same lens and is focused on the adjustable input pinhole of the tandem Fabry-Perot interferometer by a lens L of focal length 40 cm. Before reaching the interferometer the light passes through a bandpass filter BF that allows transmission of the light that has a wavelength within the range of 532 ± 5 nm. After the scattered light enters the spectrometer it is reflected towards a collimating lens and directed by a set of mirrors and prisms so it passes three times through each FPI.

To achieve resolution high enough for a measurement of Brillouin scattering a plane parallel Fabry-Perot interferometer (FPI) is used as a scanning spectrometer. In the basic form a FPI consists of two very flat, precisely parallel, highly reflecting surfaces separated by some distance d [44]. The optical spacing $L = nd$ between the mirrors of which FPI consists can be changed. The transmission is close to unity over a spectral interval $\Delta\lambda$ around a special value of a wavelength λ_n and decreases to a very low value outside this interval. The light of wavelength λ_n will be transmitted

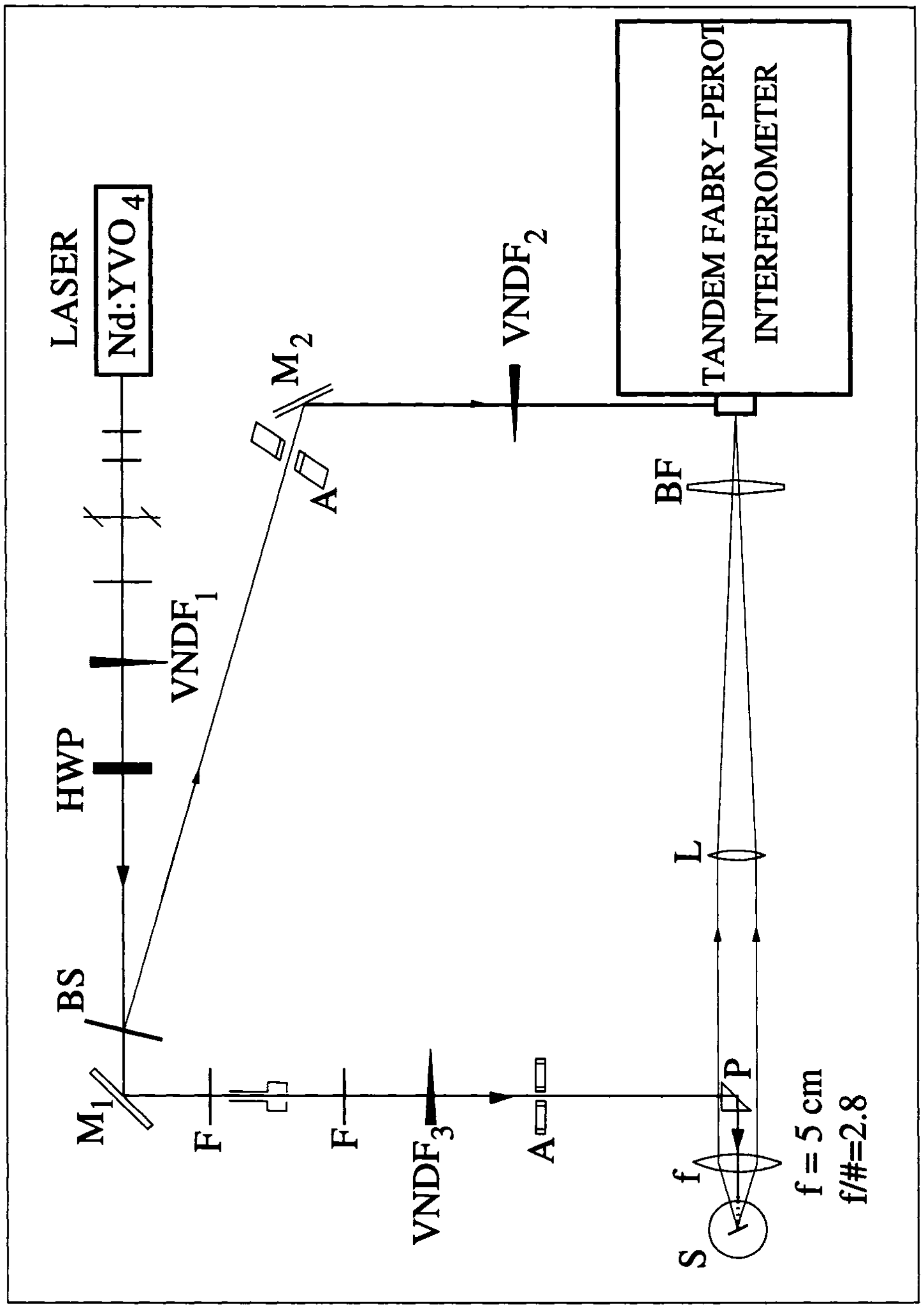

Figure 3.1: Experimental Setup. $Nd : YVO_4$ - laser, HWP - half wave plate, BS - beam splitter, M - mirror, F - filter, $VNDF$ - variable neutral density filter, A - aperture, BF - bandpass filter, L - lens, P - prism, f - focusing/collecting lens

if the following condition is fulfilled:

$$L = \frac{n\lambda_n}{2}, \tag{3.1}$$

where n is an integer. The simultaneous transmission of two incident light beams of wavelengths λ_n and $\lambda_n + \Delta\lambda$ will occur if the minimum separation of the wavelengths is

$$p\lambda_n = (p-1)(\lambda_n + \Delta\lambda). \tag{3.2}$$

Using Equation (3.1) the value by which the adjacent wavelengths are separated is found to be [46]:

$$\frac{1}{\lambda_n} - \frac{1}{\lambda_{n-1}} = \frac{1}{L}\left(\frac{n}{2} - \frac{n-1}{2}\right) = \frac{1}{2L}. \tag{3.3}$$

From Equation (3.3) the adjacent frequencies are separated by a frequency difference called free spectral range (FSR) which is given by [53]

$$FSR = \frac{c}{2L}. \tag{3.4}$$

As $L = nd$, the FSR can be changed either by varying the distance between the mirrors (piezoelectric scanning) or the refractive index of the medium between them (pressure scanning). The former method is used in the spectrometer that was part of this experimental setup.

The resolution of the FPI is determined by the width of the transmission peak. The ratio of FSR to width is the finesse F. The finesse contributes to the contrast, which is the ratio of maximum to minimum transmission. The upper limit of the contrast ($\sim$ 1000 for a single-pass FPI) is insufficient for backscattering measurements on opaque materials. To increase the upper limit two or more interferometers are placed in series or the light passes through the same interferometer more than once [47]. The optical system in the interferometer used in the present experiments is shown in Figure 3.2. It can be used in a triple-pass tandem mode for a total of six passes and a contrast of the order 10^9 [46].

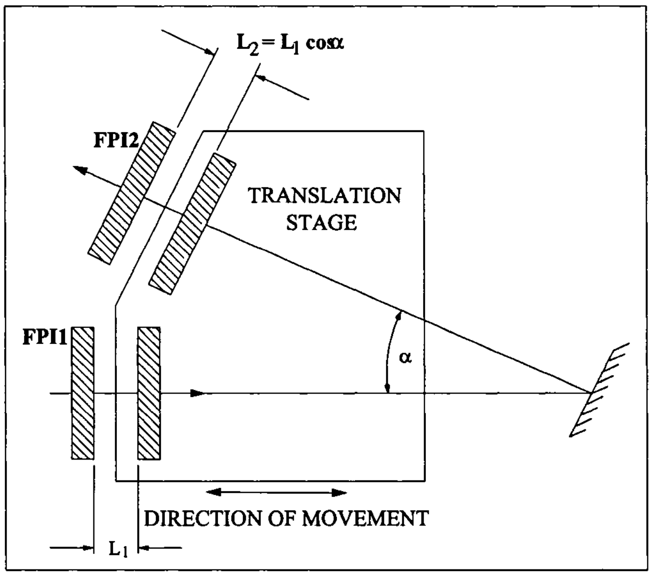

Figure 3.2: The principle of the tandem scan. $FP1$ and $FP2$ - Fabry-Perot interferometers, L_1, L_2 - optical spacing between mirrors, α - angle between two Fabry-Perot interferometers. [54] after.

To scan the transmitted wavelength it is necessary to increase the optical spacings L_1 and L_2 (see Figure 3.2) by values δL_1 and δL_2 respectively such that

$$\frac{\delta L_1}{\delta L_2} = \frac{L_1}{L_2}. \tag{3.5}$$

The condition stated by Equation (3.5) has to be fulfilled as wavelength is scanned.

The design used in the interferometer is based on the concept of a scanning stage, as shown in the Figure 3.2. The spacings of the mirrors are set so that a movement of the stage would bring both sets from simultaneous contact when $L_1 = 0$ to the spacings of L_1 and $L_1 \cos\theta$. The first Fabry-Perot interferometer $FPI1$ is set perpendicularly to the direction of stage movement. One mirror is located on the stage, the other is fixed on a separate platform. The second $FPI2$ is mounted with its optical axis at an angle α to the direction of the scan. One of the mirrors is on the scanning stage, the other is on an device which allows small translation of the mirror for adjustment. This design, apart from having large scan range, results in a tilt-free and highly linear scan [47]. In addition, it satisfies the criteria of static and dynamic synchronization. Static synchronization means that spacings of the two interferometers $FPI1$ and $FPI2$ do not vary form their correct relative value by more than 2 nm. Dynamic synchronization requires that the correct relative spacings are maintained over a scan of several micrometers [55].

3.2 Gas Handling System

The gas handling system, shown in Figure 3.3, was built to investigate the Brillouin light scattering from the sample in various gaseous environments. Gas was admitted to the system through the valve $V1$. The pressure inside the system is monitored by the pressure gauge. The most important part of the system, the sample holder is shown in the Figure 3.4. It is made primarily of brass and allows the sample to be surrounded by any gas up to pressures of ~ 1 *atm*. The sample is mounted on a rotating stage that allows one to freely set the incidence angle between 0° and 90°. The only limitation to the choice of the angle of incidence arises from the length of the window on the holder. Therefore practically the incidence angle was able to be set between 20° and 70°. A rotary vacuum pump was used to evacuate the system to a pressure of a few $\mu m\ Hg$.

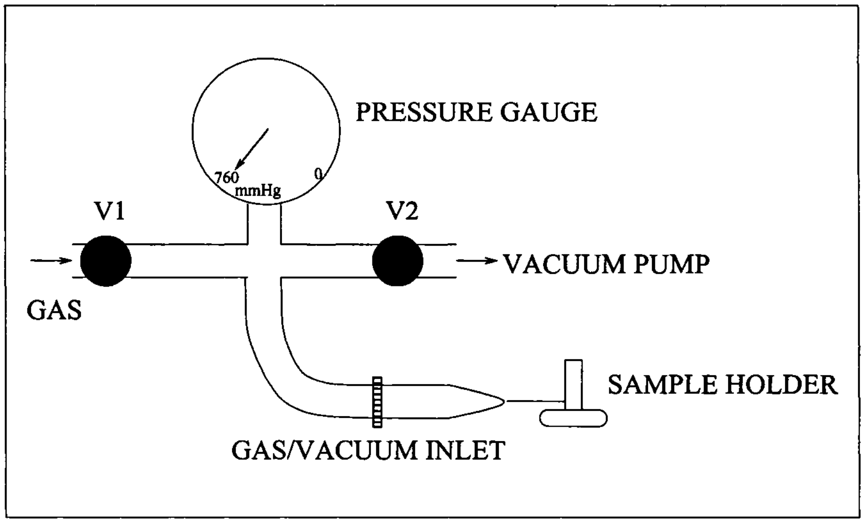

Figure 3.3: Gas handling system.

3.3 Sample Preparation

The carbon nanotube arrays used in this work were produced by J.M. Xu and coworkers at Brown University [28]. They were fabricated by pyrolysis (thermal de-

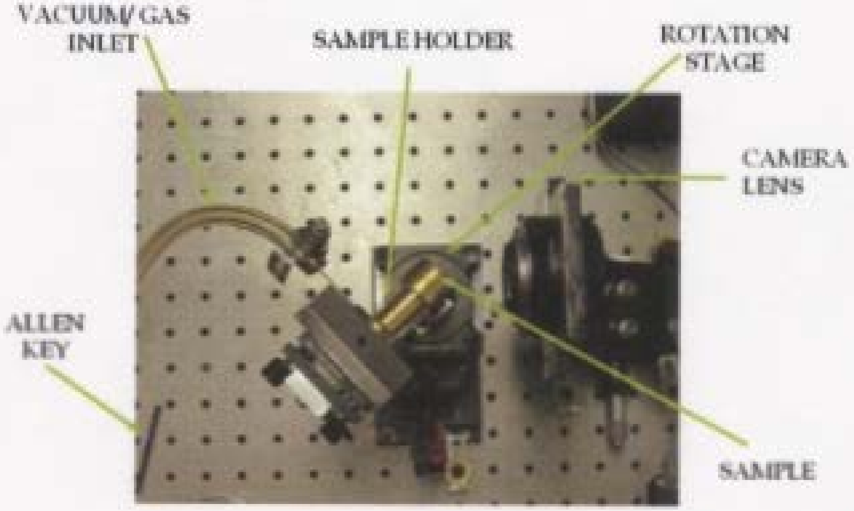

Figure 3.4: The sample holder. It connects to the rest of the system via the transparent hose.

composition [56]) of acetylene on cobalt within a hexagonal close packed nanochannel alumina template [32]. This method allows for the production of highly-ordered, large-area, two-dimensional arrays of densely packed, semiconducting and tunable in bandgap, multi-walled nanotubes, uniform in diameter, length and orientation [33].

The production begins when aluminum of high purity is anodized on the desired substrate. Appropriate anodization conditions guarantee that the pores of anodic alumina self-organize into a hexagonal array. The pores are oriented vertically and parallel to one another. The array is highly ordered and defect-free over large areas. The pore diameters, density and length in the hexagonal array can be controlled by the variation of the anodization conditions. This array acts as a template for carbon nanotube formation. The next stage in the process is the electrochemical deposition of cobalt in the bottom of the pores. Cobalt serves as a catalyst. To allow the array of nanotubes to grow the catalyst is reduced by heating the template with cobalt in a tube furnace at a temperature of 600° C under the CO flow for $4 - 5$ h. The flow rate is 100 cm^3/min. After this, the CO is replaced by a mixture of 10% C_2H_2 (acetylene) in nitrogen at the same flow rate. Typically, the C_2H_2 flow is kept for 2 h at a temperature of 650° C. The samples are then annealed in nitrogen at the same temperature for 15 h.

3.4 Samples

Schematic pictures of all the samples studied are presented in Figure 3.5. Two carbon nanotube arrays and two samples representing intermediate stages in fabrication process were investigated. The latter two were used to help distinguish between Brlillouin peaks originating from nanotube array and those from alumina template.

The samples representing initial stages of the production process, alumina templates, were investigated in order to complete the study of carbon nanotube arrays.

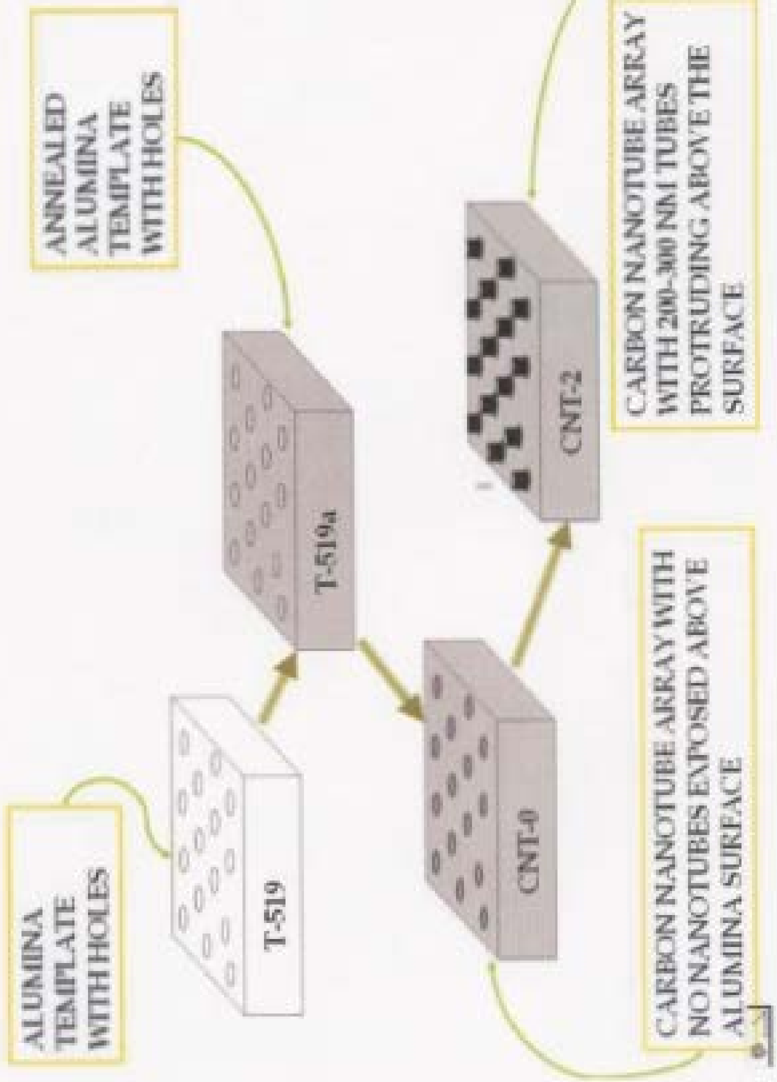

Figure 3.5: Schematic pictures of the samples studied in the experiment with descriptions.

The first one, labeled $T-519$, is the result of the first stage of production. It is an anodized alumina template with holes arranged in close-packed hexagonal array. The second sample that was examined, $T-519a$, was an annealed alumina template with holes. The sample referred to as $CNT-0$ is a carbon nanotube array formed on an anodized alumina template with the top of the nanotubes flush with the top of the alumina template. The sample called $CNT-2$ is also a carbon nanotubes array formed on an anodized alumina template but with the length of the nanotubes exposed by etching the alumina matrix with a mixture of chromic and phosphoric acid. The total length of the nanotubes occupying the pores in the alumina is 6 μm, $200-300$ nm of which protrudes above the surface of the template. This sample was also annealed with an Ar^+ laser at a power of 4 W for 5 minutes to reduce brittleness.

A scanning electron microscope image of an array of multi-walled carbon nanotubes (sample referred to as $CNT-2$) is presented in Figure 3.6. It can be seen that all of the nanotubes in the array are parallel to one another and are oriented perpendicularly to the template, forming A close-packed hexagonal array. All of them are open-ended and of the comparable length and diameter. The mean outer diameter of an individual tube, read from the SEM image is ~ 50 nm.

Chapter 4

Results and Discussion

All Brillouin scattering experiments were made for a finite range of θ_s centered around θ_i (in other words in 180° backscattering geometry [47]). Unless specified otherwise, the experimental conditions were as follows: room temperature ($\sim 293K$), ~ 9 h collection time (50000) scans, incident beam power of 40 mW and the incident light polarized in the plane of incidence.

As was mentioned earlier, the samples were surrounded by various gases to study the influence of the environment on the Brillouin spectrum of carbon nanotube arrays (*i.e.*, the presence of the gas might alter the frequencies of the vibrational modes of the nanotubes). The molecular masses and polarizabilities (proportionality factor between the dipole moment induced in an atom, molecule, or a particle and the inducing electric or magnetic field [57]) of these gases are summarized in Table 4.1.

The first of the investigated samples was an ordered carbon nanotube array with $\sim 5\%$ of the total length of the nanotubes protruding above the surface of the

Table 4.1: Masses and polarizabilities of the gases used as environments [58].

Gas	**Mass** $[10^{-3}\mathrm{kg/mol}]$	**Polarizability** $[10^{-23}\mathrm{cm}^3]$
Vacuum	0	–
H_2	2.0158	0.804
CH_4	16.04	2.593
Air	28.89019	1.74
Ar	39.948	1.641
Kr	83.8	2.484
CF_4	87.98612	3.838
C_2F_6	137.98418	6.54
SF_6	146.05	6.82

alumina template $(CNT-2)$. Brillouin spectra at an FSR from 50 to 8 GHz were collected in vacuum and various gaseous environments to investigate the effect of gas on the Brillouin spectra of carbon nanotube arrays and therefore on the elastic properties of the array. Additionally Brillouin spectra in air and vacuum were collected from a control samples: *(i)* non-annealed alumina template with holes arranged in a hexagonal, close-packed array $(T-519)$, *(ii)* an annealed alumina template with holes $(T-519a)$ and *(iii)* highly-ordered carbon nanotube array with the top of the nanotubes flush with the surface of the alumina template $(CNT-0)$. The latter three samples were studied to aid in the determination of the origin of the modes observed in the spectra collected from $CNT-2$.

4.1 Spectra collected at an FSR of 50 GHz

4.1.1 Carbon nanotube array with 200 – 300 *nm* of the nanotubes protruding above the alumina surface

A typical Brillouin spectrum of $CNT-2$ collected at an FSR of 50 GHz is presented in Figure 4.1. It was collected in air with a 60° angle of incidence. Analysis of this spectrum showed two peaks, one at around 6 GHz (assigned the label B_6) and one at 32 GHz (B_{32}). The latter peak was found to originate from the cover slip serving as a window on the sample holder (the sample and window were located very close to one another) and therefore will not be discussed further.

The investigation of the data was focused on the region where the peak labeled as B_6 was located. In Figure 4.2 the Brillouin spectra collected from $CNT-2$ in various gases with $\theta_i = 30°$ and $\theta_i = 60°$ are compared. When the incident angle θ_i was set to 60° the peak observed at $B_6 \sim 6$ GHz was found to be very broad and of low intensity. Fitting a single Lorentzian to peak B_6 in the spectrum collected in air resulted in a low value of the correlation coefficient and therefore the fit was not acceptable. Based on this result the presence of two different peaks was suspected. This prediction could not be confirmed without doubt as the peak resolution is not sufficient. The same phenomenon was observed when spectra of $CNT-2$ in other gases (apart from spectra collected in H_2 environment) and in vacuum were analyzed. With the change of the incident angle θ_i the changes in intensities and frequency shifts

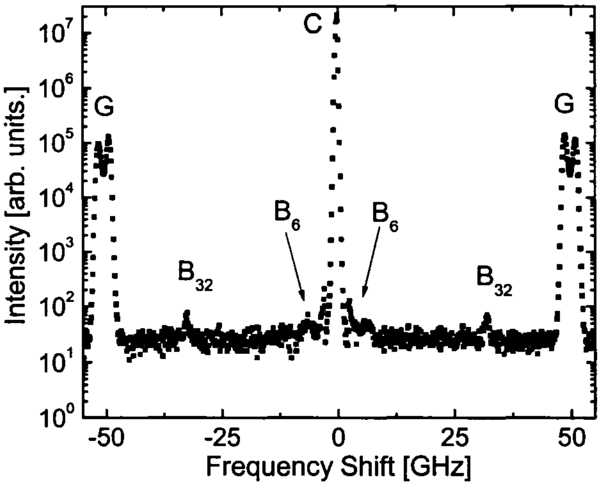

Figure 4.1: Brillouin spectrum of $CNT-2$ at an FSR of 50 GHz in air with a 60° angle of incidence. C - elastically scattered light, G - ghosts, B_6, B_32 - Brillouin peaks.

allow one to distinguish two separate peaks at frequency shifts of ~ 5 GHz and ~ 7 GHz, labeled B_5 and B_7, respectively.

As can be seen in Fig 4.2, the spectra from $CNT-2$ in most of the gases and vacuum do not differ from one another, especially with $\theta_i = 30°$. The only exception, as already mentioned, is the spectrum collected from $CNT-2$ in H_2, where the peak B_5 is more intense. The maximum intensity of the peaks decreases with increasing value of θ_i which makes resolution of two peaks impossible when $\theta_i = 60°$ and caused the ambiguity in determination of the number of peaks observed. What is more, the frequency shift of the peak B_7 varies depending on the gas surrounding the

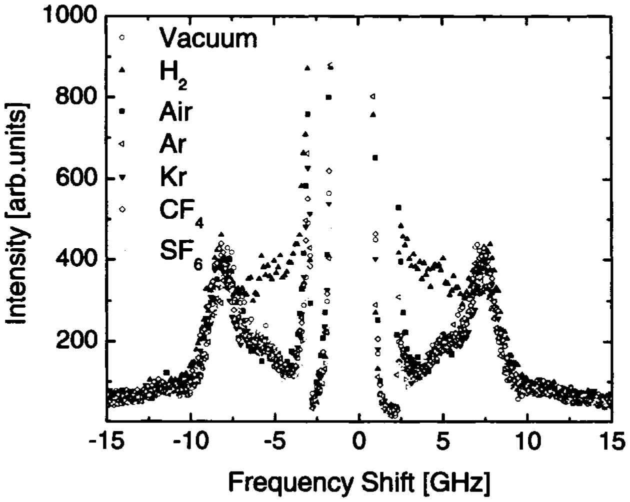

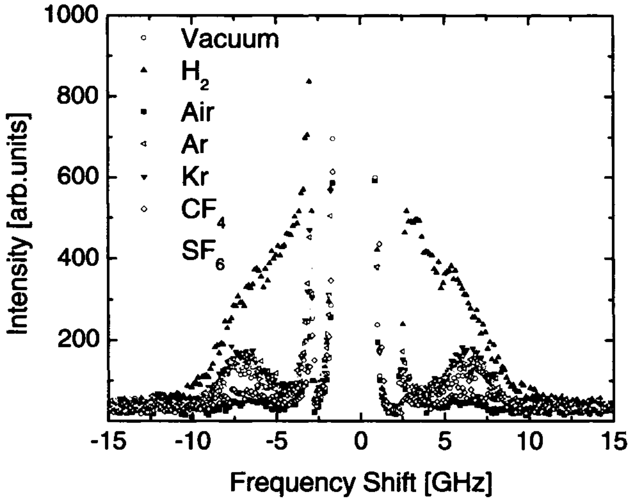

Figure 4.2: Brillouin spectra of $CNT-2$ at an FSR of 50 GHz in various gases with a 30° angle of incidence (top) and 60° angle of incidence (bottom).

sample. The difference in the shape and intensity of B_5 and B_7 in the spectrum from $CNT-2$ while surrounded by H_2 is especially well seen when θ_i is 60°. The detailed analysis of spectra from $CNT-2$ in various gases is presented below. The integrated intensities, frequency shifts, $FWHM$ and maximum intensities of the peaks B_5 and B_7 in $CNT-2$ with different angles of incidence and in various gaseous environments are summarized in Table 4.2. The values were obtained by averaging the Stokes and anti-Stokes data. The uncertainty in these values is simply the standard deviation.

The electronic properties of the nanotubes were reported to be affected by certain gases surrounding the sample. O_2 is found to be adsorbed by nanotubes changing their resistance [18], [22] and transforming small-gap semiconducting nanotubes into metallic ones [19], [20]. N_2 and He change the resistance of the nanotubes, however the exposure to these gases influences the electronic properties less significantly than in case of O_2 [22]. H_2 is also easily adsorbed [23], [24] and can be stored inside the tubes. To examine whether the Brillouin spectrum, and hence the elastic properties, exhibit any sort of sensitivity to the gas to which they are exposed the set of gases of various masses and polarizabilities were chosen. The reference spectra were collected from the sample placed in vacuum. These spectra were collected with the incident angle ranging from 30° to 70°. This set of experiments allows one to determine whether the observed modes are of surface or bulk character as well as permits estimation of phonon velocities. The surface mode velocity is expected to exhibit the linear dependance on the $\sin\theta_i$ according to Equation (2.28) whereas the velocities of bulk modes

Table 4.2: Integrated intensities, frequency shifts, $FWHM$ and maximum intensities of the peaks B_5 and B_7 in $CNT-2$ in various gaseous environments.

Gas	**B$_i$**	θ_i [°]	**Integrated Intensity** [arb.units × GHz ×10^3]	**Frequency Shift** [GHz]	**FWHM** [GHz]	**Maximum Intensity** [arb.units ×10^2]
Vac.	B_5	30	0.60 ± 0.31	5.55 ± 0.30	3.50 ± 0.09	1.08 ± 0.03
		40	0.20 ± 0.05	5.02 ± 0.28	2.21 ± 0.53	0.57 ± 0.02
	B_7	30	0.91 ± 0.02	7.55 ± 0.33	1.68 ± 0.04	3.45 ± 0.01
		40	0.99 ± 0.01	7.28 ± 0.36	2.57 ± 0.04	2.44 ± 0.04
		50	1.04 ± 0.01	6.74 ± 0.34	2.79 ± 0.08	2.38 ± 0.03
		60	0.61 ± 0.02	6.69 ± 0.31	3.51 ± 0.19	1.11 ± 0.01
Air	B_5	30	4.57 ± 0.03	5.40 ± 0.31	3.07 ± 0.41	0.96 ± 0.07
		40	0.61 ± 0.18	5.49 ± 0.24	4.20 ± 0.16	0.93 ± 0.27
	B_7	30	0.94 ± 0.02	7.73 ± 0.34	1.85 ± 0.04	3.22 ± 0.03
		40	0.79 ± 0.09	7.27 ± 0.26	2.15 ± 0.13	2.29 ± 0.18
		50	1.06 ± 0.03	6.79 ± 0.37	3.08 ± 0.04	2.50 ± 0.27
		60	0.10 ± 0.01	6.22 ± 0.30	2.46 ± 0.04	0.30 ± 0.04
Ar	B_5	30	0.46 ± 0.01	5.16 ± 0.26	2.75 ± 0.01	1.06 ± 0.03
		40	0.49 ± 0.13	5.08 ± 0.23	4.22 ± 0.80	0.73 ± 0.06
	B_7	30	0.85 ± 0.01	7.56 ± 0.30	1.85 ± 0.02	2.94 ± 0.02
		40	0.79 ± 0.6	7.38 ± 0.30	2.80 ± 0.08	1.79 ± 0.08
		50	0.99 ± 0.02	6.72 ± 0.33	3.12 ± 0.04	2.01 ± 0.01
		60	0.66 ± 0.02	6.48 ± 0.33	3.29 ± 0.06	1.24 ± 0.07
Kr	B_5	30	0.58 ± 0.02	5.48 ± 0.27	3.47 ± 0.23	107 ± 3
		40	8.86 ± 0.01	6.31 ± 0.45	3.72 ± 0.11	152 ± 6
	B_7	30	7.49 ± 0.04	7.95 ± 0.36	1.57 ± 0.03	3.04 ± 0.09
		40	0.38 ± 0.01	7.78 ± 0.36	1.79 ± 0.03	1.36 ± 0.06
		50	0.84 ± 0.07	6.73 ± 0.33	3.07 ± 0.35	1.75 ± 0.06
		60	0.74 ± 0.01	6.58 ± 0.37	3.24 ± 0.08	1.45 ± 0.02
CF$_4$	B_5	30	0.49 ± 0.07	5.46 ± 0.28	3.04 ± 0.43	1.02 ± 0.01
		40	0.87 ± 0.08	6.48 ± 0.46	3.48 ± 0.06	1.60 ± 0.12
		50	0.83 ± 0.08	6.48 ± 0.32	3.50 ± 0.12	1.58 ± 0.10
	B_7	30	0.91 ± 0.03	7.86 ± 0.38	1.67 ± 0.01	3.45 ± 0.10
		40	0.27 ± 0.03	7.82 ± 0.37	1.36 ± 0.06	1.25 ± 0.09
		50	0.29 ± 0.03	7.82 ± 0.24	1.40 ± 0.06	1.29 ± 0.09
SF$_6$	B_5	30	0.56 ± 0.01	5.38 ± 0.29	3.13 ± 0.05	114 ± 4
		50	0.80 ± 0.02	6.09 ± 0.28	2.88 ± 0.08	1.76 ± 0.01
		60	0.52 ± 0.01	6.09 ± 0.42	2.89 ± 0.01	1.14 ± 0.01
	B_7	30	0.85 ± 0.02	7.64 ± 0.38	1.85 ± 0.01	2.92 ± 0.09
		50	0.25 ± 0.03	7.33 ± 0.35	1.09 ± 0.11	1.43 ± 0.04
		60	0.04 ± 0.02	7.45 ± 0.33	0.66 ± 0.28	0.41 ± 0.05

are independent of the angle of incidence.

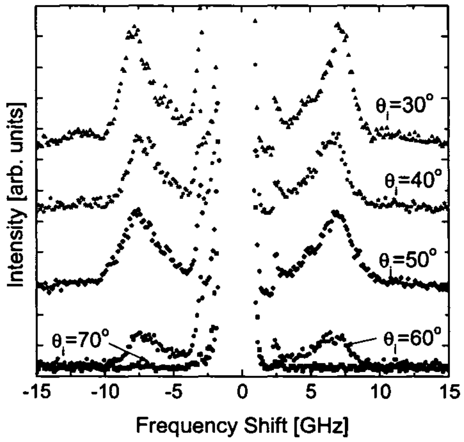

Figure 4.3: Brillouin spectra of $CNT-2$ at an FSR of 50 GHz in vacuum with different angles of incidence (as indicated).

As can be seen in Figure 4.3, the maximum intensity of the peak B_7 decreases with increasing angle of incidence so that no peaks can be distinguished when the angle of incidence is 70°. An increase of the peak's $FWHM$ is observed when θ_i is increased. This is probably an effect of the overlapping of the two peaks which in spectra collected with higher angle of incidence prevents the resolution of B_5. Because of that, the integrated intensity cannot really serve as a useful piece of information. The peak B_5 could only be resolved for the two lowest angles of incidence and the integrated intensity is associated with a high uncertainty for the spectrum collected with a 40° angle of incidence.

Figure 4.4 shows the dependence of the frequency shift of peaks B_5 and B_7 on the $\sin\theta_i$. The frequency shift for the peak B_7 exhibits the same trend of decreasing frequency shift with increasing θ_i. Having only two values (see Table 4.2) for the frequency shift of the peak B_5 means that no trend can be specified.

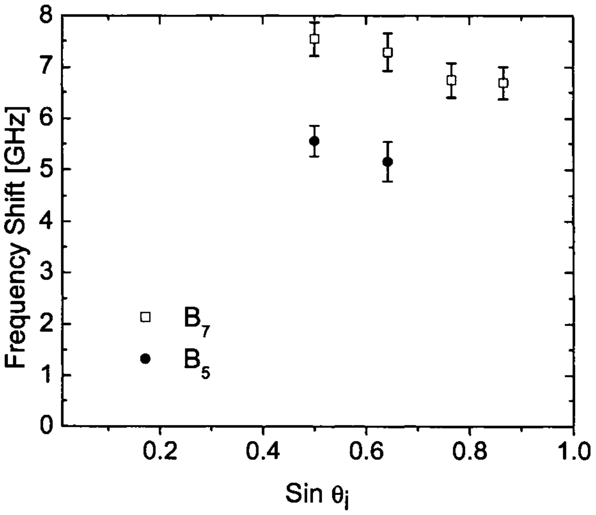

Figure 4.4: Plot of frequency shifts of peaks B_5 and B_7 (as indicated) versus the $\sin\theta_i$ in vacuum.

In Figure 4.5 spectra collected in air at an FSR of 50 GHz with the five different angles of incidence varying from 30° to 70° are compared. With the lower angles of incidence ($\theta_i = 30°$ and $\theta_i = 40°$) the presence of two peaks of different intensities is evident. Peak B_7 is of higher maximum intensity, and its intensity decreases with increasing angle of incidence but there is no obvious trend. In the spectra collected with $\theta_i = 50°$ and $\theta_i = 60°$ the resolving of the two peaks is impossible due to the overlapping and decrease in intensity.

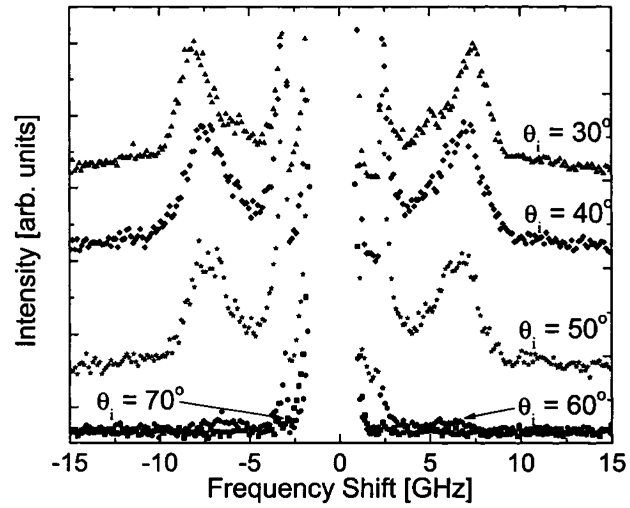

Figure 4.5: Brillouin spectra of carbon nanotube array at an *FSR* of 50 *GHz* in air with different angles of incidence (as indicated).

The trend in angular dependence of the frequency shifts of peaks B_7 and B_5 is similar to that observed in vacuum (Figure 4.4). The frequency shift of B_7 decreases with increasing angle of incidence. The value of frequency shift for B_7 for $\theta_i = 30°$ is 20% larger than that obtained for $\theta_i = 60°$. This means that this peak is not due to a surface mode since the frequency shift of such a mode increases with increasing angle of incidence (see Equation 2.28). It could, however, be due to a bulk acoustic mode. The other peak (B_5) can be observed only in two spectra, corresponding to the lowest angles of incidence and its frequency shift and maximum intensity are independent of θ_i. The fact that the frequency shift of peak $B-5$ is independent on the angle of incidence suggests that this peak could result from a bulk mode.

The spectra of $CNT-2$ surrounded by the rare gases Ar and Kr and collected for various angles of incidence are presented in Figure 4.6. The plot of frequency shifts versus the $\sin\theta_i$ is presented in Figure 4.7. The behavior of the peak B_7 is exactly the same in both gases - the frequency shift decreases with increasing angle of incidence leading eventually to the overlap of both peaks and resulting in the difficulties of resolving the peak labeled as B_5. This trend is the same as described for the other spectra and in this cases is even more evident. The broadening of the peak B_7 with increasing angle of incidence is observed both in the spectra collected from the carbon nanotube array in Kr environment and in Ar. When the sample is surrounded by Kr, the frequency shift for the peak labeled B_5 with $\theta_i = 40°$ is significantly higher. The problem with resolving both peaks with increasing angle of incidence results in no confirmation whether the integrated intensity is a significant feature.

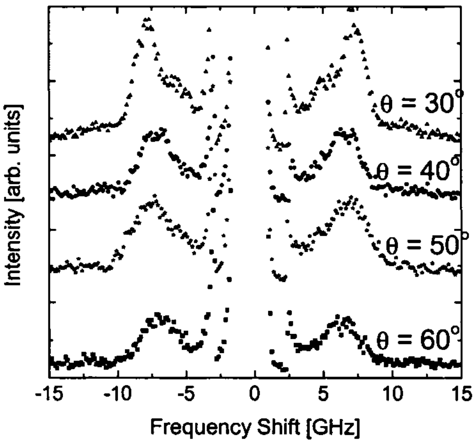

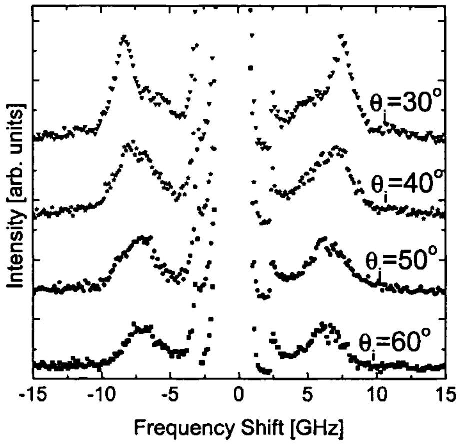

Figure 4.6: Comparison of spectra of carbon nanotube array at an *FSR* of 50 *GHz* in *Ar* (top) and in *Kr* (bottom) with different angles of incidence (as indicated).

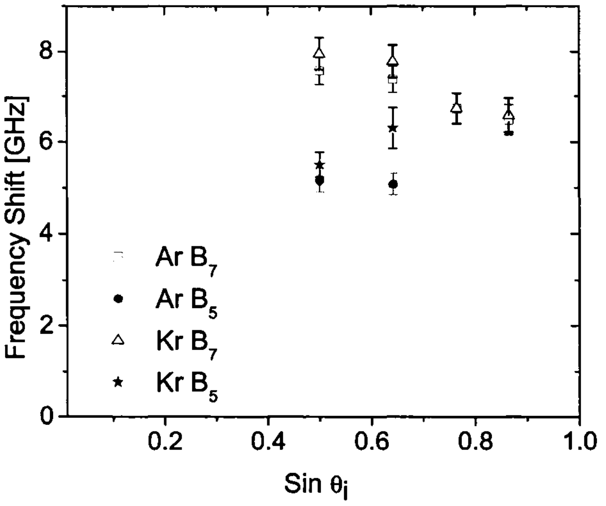

Figure 4.7: Plot of frequency shifts of peaks B_5 and B_7 (as indicated) versus the $\sin\theta_i$ in Ar and Kr.

Brillouin spectra were also collected from $CNT-2$ surrounded by CF_4 and SF_6, as presented in Figures 4.8 and 4.9. The integrated intensities, frequency shifts, $FWHM$ and maximum intensities are summarized in Table 4.2.

Tetrafluoromethane (CF_4) is a gas of molecular mass comparable to that of Kr but of higher polarizability (see Table 4.1). Unlike in the case of spectra of $CNT-2$ in air, rare gases and vacuum, the frequency shift of peak B_7 is independent of θ_i. The frequency shift of peak B_5 varies with θ_i, but the character of the angular dependence is unclear. Both peaks are clearly seen up to an angle of incidence of 50°, and no increase of the $FWHM$ in any of the peaks is observed with increasing θ_i.

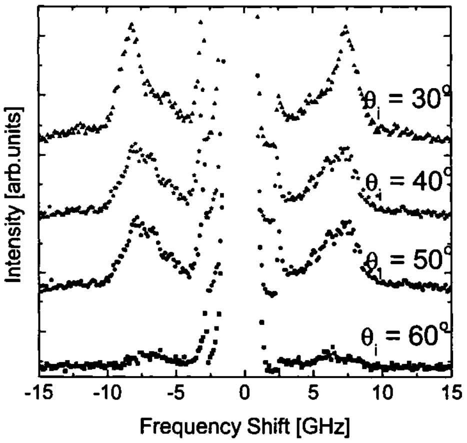

Figure 4.8: Brillouin spectra of carbon nanotube array at an FSR of 50 GHz in CF_4 with different angles of incidence (as indicated).

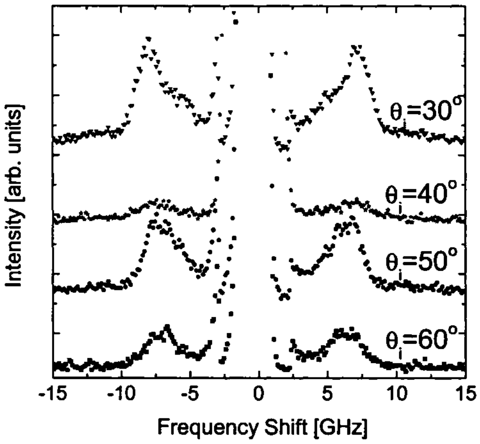

Figure 4.9: Brillouin spectra of carbon nanotube array at an FSR of 50 GHz in SF_6 with different angles of incidence (as indicated).

Sulfur hexafluoride (SF_6) is a gas of mass and polarizability significantly higher than any other gas discussed so far (see Table 4.1). The plot of angular dependence of frequency shifts is shown in Figure 4.10. As for CF_4, the peak B_7 seems to remain at a fixed frequency shift whereas the position of the inner peak varies (see Table 4.2). This behavior of B_5 resembles that observed in Kr (Figure 4.7) and in CF_4, which could suggest that it is characteristic for heavier gases. When the carbon nanotube array is in SF_6 both peaks are visible up to 60° angle of incidence. The $FWHM$ of B_7 decreases significantly with increasing θ_i - the value of $FWHM$ for spectrum collected with 60° angle of incidence is equal to $\sim$ 30% of the value obtained with $\theta_i = 30°$.

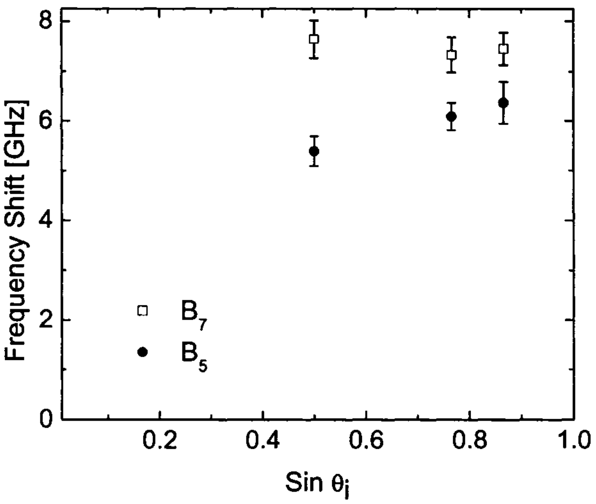

Figure 4.10: Plot of frequency shifts of peaks B_5 and B_7 (as indicated) versus the $\sin\theta_i$ in SF_6.

An interesting and unexpected feature for the spectra collected when $CNT-2$ is in SF_6 is the intensity of the peaks B_5 and B_7 when the angle of incidence is 40° (see Figure 4.9). The data for this spectrum is not obtained as the profile of the peak neither resembles a Lorentzian function in the region of interest nor can it be distinguished as multiple peaks. This feature does not seem to be of a significance - probably results from the choice of spot on the sample or imperfections in the alignment of the interferometer.

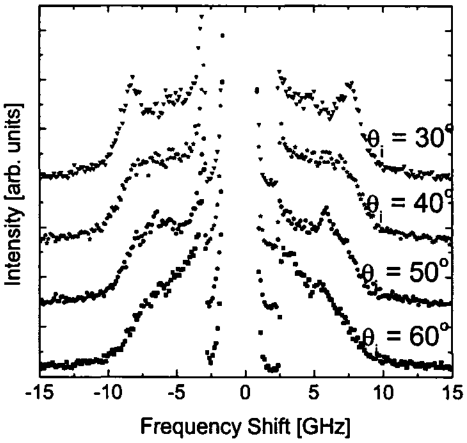

Figure 4.11: Brillouin spectra of carbon nanotube array at an FSR of 50 GHz in hydrogen with different angles of incidence (as indicated).

Figure 4.11 shows spectra collected from $CNT-2$ when surrounded by H_2. The values of integrated intensity, frequency shift, $FWHM$ and maximum intensity are summarized in Table 4.3. Spectra collected from the carbon nanotube array in the H_2 environment are qualitatively different from other spectra presented here. Two overlapping peaks are present, one of which (B_5) is very close to the central elastic peak. The shoulder of elastic peak causes the inner peak to be cut off and the fitting procedure results in high uncertainties associated with the evaluated parameters. As in other gases, the higher the angle of incidence the less distinguishable are the peaks. The frequency shifts of both B_5 and B_7 peaks decrease with the increasing angle of incidence as can be seen in Figure 4.12.

Table 4.3: Integrated intensities, frequency shifts, *FWHM* and maximum intensities of the peaks of $CNT-2$ in H_2.

Gas	**B_i**	**θ_i [°]**	**Intensity [arb.units × GHz $\times 10^3$]**	**Shift [GHz]**	**FWHM [GHz]**	**Intensity [arb.units $\times 10^2$]**
H_2	30	B_5	2.73 ± 0.4	4.58 ± 0.34	5.11 ± 0.04	3.40 ± 0.02
	40		1.77 ± 0.84	4.27 ± 0.46	3.64 ± 1.30	2.95 ± 0.42
	50		1.19 ± 0.28	3.59 ± 0.14	3.08 ± 0.62	2.44 ± 0.08
	30	B_7	0.74 ± 0.01	7.95 ± 0.32	1.65 ± 0.01	2.85 ± 0.01
	40		1.51 ± 0.43	7.14 ± 0.17	3.54 ± 0.52	2.65 ± 0.39
	50		1.83 ± 0.01	6.43 ± 0.35	3.81 ± 0.18	3.07 ± 0.17
	60		1.22 ± 0.23	6.33 ± 0.54	3.43 ± 0.26	2.25 ± 0.25

This trend in only observed when the sample is surrounded by H_2. What is more the label B_5 attached to the inner peak is more symbolic as the largest frequency shift at $\theta_i = 30^o$ is less that 5 GHz, as presented in Table 4.3. The maximum intensities of the peaks are at least twice as big as those evaluated for $CNT-2$ in vacuum. Apart from the difference noticed between 30° and 40° in the width of B_5 and B_7, the *FWHM* seems to be independent of θ_i. This difference is probably due to the fact that when the angle of incidence is 30° the peaks overlap and the process of resolving is difficult. The ratio of the integrated intensities of the B_7 and B_5 seems to increase with increasing angle of incidence. Unfortunately, the values of integrated intensity obtained for $\theta_i = 40°$ are associated with large uncertainty value. Also, only three data points are available because peak B_5 could not be resolved and analyzed in case of $\theta_i = 60°$.

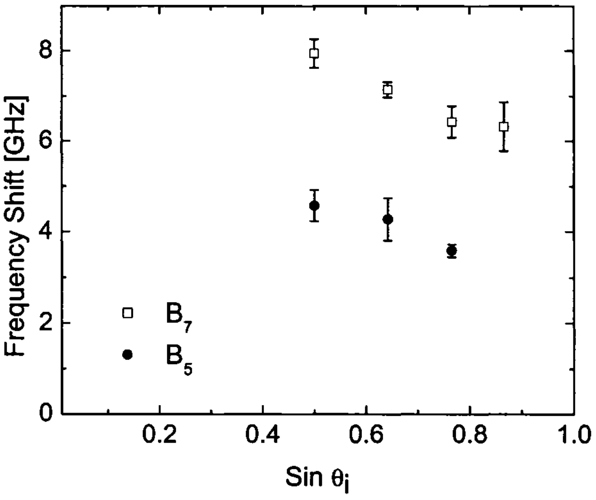

Figure 4.12: Plot of frequency shifts of peaks B_5 and B_7 (as indicated) versus the $\sin\theta_i$ in H_2.

The choice of investigating the behavior of Brillouin spectra when carbon nanotube arrays are exposed to different gases was justified by contradictory reports about the gas sensitivity of carbon nanotubes. As previously discussed in the "Introduction" there is no consensus among the authors [4], [19] - [22] about the influence of the certain gases on the properties of carbon nanotubes. The presence of a fluid around the microtubules, the counterparts of the nanotubes, can lead to the qualitative change in the dispersion relation [59]. The coupling between shell and the fluid changes the frequencies of vibrations of the tubes and the frequency dependence of the phonon vector. Although the model proposed in the cited work is presented for microtubules, both materials can be modeled as cylindrical shells [60]. The similarities are significant and the prediction that the presence of the fluid around the nanotubes can affect not only their electrical but also elastic properties seems worth further investigations.

The spectrum that is under absolutely no influence of any gas is the one collected in vacuum. The characteristic features of this spectrum are: no angular dependence of the frequency shift of peak B_5 and decreasing the frequency shift of peak B_7 with the increasing angle of incidence. Such behavior could suggest that these peaks represent bulk modes in the carbon nanotube array. The same angular dependence of the frequency shift of peaks B_5 and B_7 as described for $CNT-2$ in vacuum is observed in the rare gases and in air. The value of the frequency shift of B_5 remains the same while carbon nanotubes are exposed to these gases. This behavior could suggest that neither air nor rare gases influence the elastic properties of carbon nanotubes. The only exception that is noticed while evaluating the frequency shifts is the change of the frequency shift of the inner peak in a Kr environment. As the only difference between two rare gases, Ar and Kr, that may be meaningful in this study, is their molecular mass (see Table 4.1), the noticed variation in angular dependence of frequency shift may result from this. One data point is, however, not enough to draw a conclusion.

The same shape of the spectra (*i.e.* two peaks at frequency shift of 5 and 7 GHz of intensities that decrease with increasing angle of incidence), but slightly different behavior of the peaks were noticed during investigation of the modes in heavier gases of higher polarizability: the shift of the peak B_5 does not change while the B_7 one exhibits an increase of frequency shift with increasing angle of incidence. The increase is not big enough to state that the peak B_7 can be classified as a surface mode. The behavior of the frequency shift of peaks B_5 and B_7 when $CNT-2$ is surrounded by CF_4 and SF_6 could confirm the prediction that the mass of the gas creating the environment around the carbon nanotube array may influence the angular dependence of the frequency shifts. As can be seen in Figure 4.10 the frequency shift is independent of $\sin\theta_i$ and hence B_5 and B_7 could be bulk modes.

The spectrum collected from the carbon nanotube array in H_2 is qualitatively different (*i.e.*, significantly different values of the frequency shift of peak B_5, its angular dependency and higher intensity). No linear dependence on $\sin\theta_i$ suggests that both B_5 and B_7 are bulk modes although the presence of the H_2 increases the intensity of the peaks and decreases the values of frequency shifts. These features could suggest that H_2 does not leave the elastic properties of nanotubes unaffected. This observation may lead to agreement with theories that suggest the adsorption and chemisorption of hydrogen to the nanotubes [61] and its effect on the properties of the tubes. We may observe the storage of hydrogen inside the tubes [23] or adsorption of hydrogen molecules on the surface of the tubes. As all experiments were performed in room temperature it is unlikely that chemisorption occurred. None of the gases permanently affected the $CNT-2$ sample as the spectrum collected in vacuum after $CNT-2$ was exposed to various gases is the same as one collected before. The subject of the gas sensitivity of nanotubes is still an area of active research.

4.1.2 Carbon nanotube array with nanotubes flush with alumina surface

The spectra of carbon nanotube arrays with the top of the nanotubes flush with the top surface of the alumina template were collected at an FSR of 50 GHz for twice as long as those of carbon nanotubes with $200-300$ nm exposed (100000 scans), as the response signal was very low and after 50000 scans the peaks were of too low intensity to be positively identified. Even in the 100000-scan spectra, the peaks are still very weak but their presence is noted on both sides of the central elastic peak in some of them. This confirms that they are Brillouin doublets. As these data were collected as a supplementary to the research of $CNT-2$ only two environments (air and vacuum) were investigated.

The sample ($CNT-0$) was exposed to vacuum (Figure 4.13 top) and air (Figure 4.13 bottom). The obtained Brillouin spectra were not significantly different from each other, apart from the lower and less scattered background observed in spectra collected when $CNT-0$ was surrounded by vacuum. Only two peaks are observed

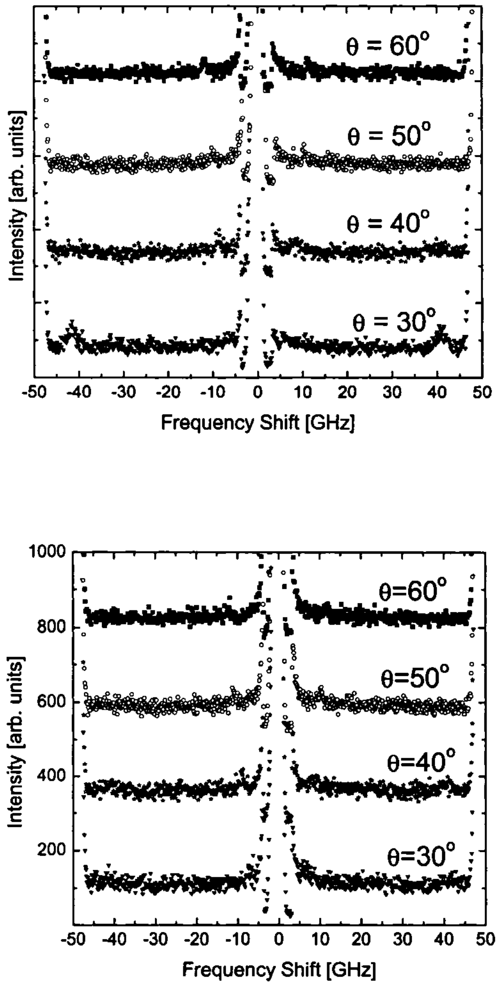

Figure 4.13: The spectra of $CNT-0$ in vacuum (top) and in air (bottom) at an FRS of 50 GHz and with various angles of incidence (as indicated).

throughout all range of incident angles: one at a frequency shift of ~ 11 GHz on the spectra with higher incidence angle and one around 40 GHz in the spectrum collected at with $\theta_i = 30°$. The peaks are labeled B_{11} and B_{40} respectively. Table 4.4 collects the values of frequency shifts for the modes seen in $CNT - 0$ sample.

Table 4.4: Frequency shifts for $CNT - 0$ in vacuum.

θ_i [°]	$\mathbf{B_{11} \pm \delta B_{11}}$ **[GHz]**	$\mathbf{B_{40} \pm \delta B_{40}}$ **[GHz]**
30	–	41.27 ± 0.29
40	8.46 ± 0.11	–
50	10.15 ± 0.27	–
60	11.66 ± 0.24	–

The surface mode observed in $CNT - 0$ was identified as originating from the alumina template with nanotubes in holes as was not observed in any of the spectra collected form $CNT - 2$. The mode at constant frequency shift of ~ 40 GHz that is observed only with the incidence angle of 30° was more confusing. The work by C.E. Bottani [34] reports the existence of a mode of frequency shift comparable to this one. The experimental conditions described in cited paper are very different from used in the current work. In the present experiment in $CNT - 0$ the multi-wall tubes are flush with the surface of the template and no length of the tubes are protruding, whereas in the cited work the outer sides of single wall nanotubes were scattering the light. The only thing that is the same for both experiments is an angle between tube axis and incident light. What is more, there is no evidence of a mode at ~ 40 GHz in the spectra collected for $CNT - 2$.

4.1.3 Alumina templates with holes

Two alumina templates were investigated in order to complete the study of carbon nanotube arrays. The first one ($T-519$) is an alumina template with holes arranged in close packed hexagonal array. The second sample that was studied, $T-519a$, was an annealed alumina template with holes. All spectra were collected at an FSR of 50 GHz.

A sample Brillouin spectrum collected with a 60° angle of incidence is presented in Figure 4.14. Three peaks can be distinguished: one well defined around 12 GHz, one around 23 GHz and one broad and hard to identify at $\sim$ 41 GHz. The exact values of frequency shifts obtained from this spectrum are summarized in the Table 4.5.

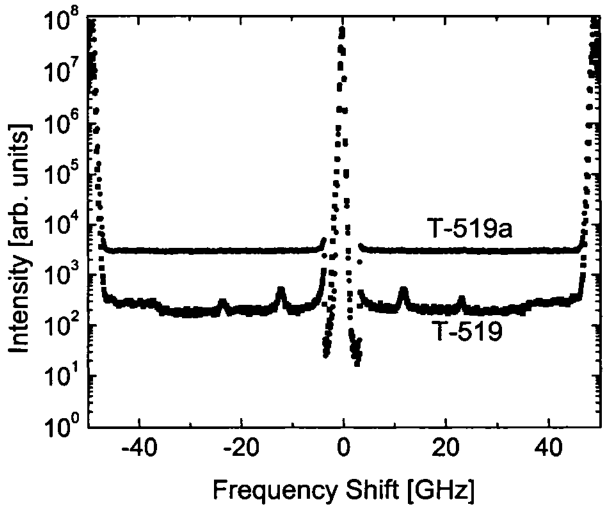

Figure 4.14: Brillouin spectra of $T-519$ and $T-519a$ at an FSR of 50 GHz and with a 60° angle of incidence.

Table 4.5: Frequency shifts for alumina template with holes (T-519).

θ_i [°]	$Al_1 \pm \delta Al_1$ [GHz]	$Al_2 \pm \delta Al_2$ [GHz]	$Al_3 \pm \delta Al_3$ [GHz]	$Al_4 \pm \delta Al_4$ [GHz]
20	5.27 ± 0.53	–	–	42.80 ± 0.26
30	6.77 ± 0.27	11.46± 0.11	23.35 ± 0.40	42.07 ± 0.28
40	8.91 ± 0.24	15.27 ± 0.25	23.42 ± 0.23	43.42 ± 0.09
50	10.66 ± 0.23	–	23.40 ± 0.24	42.77 ± 0.20
60	11.99 ± 0.22	–	23.34 ± 0.24	41.41 ± 0.41

In the case of the annealed alumina template the spectra were expected to be similar to those collected from $T-519$. No Brillouin peaks were observed in this case, however, due to an intense background (see Figure 4.14). This is the reason that none of the peaks can be identified with certainty. The origin of such a high background might be the reflectivity of the sample or it might be the result of undesirable changes in the properties of the material caused by the annealing process (*e.g.* creation of grains on the surface of the sample).

To investigate the observed peaks the spectra with different incident angles were collected and are presented in the Figure 4.15. When the value of the incident angle was changed to 30° and 40° in addition to those peaks mentioned above, one more peak was observed. Its presence can be noticed with the incident angle of 50° but its intensity is not high enough to obtain a credible fit. When the angle of incidence is set to be 20° the peak is too close to the laser line and cannot be distinguished. With the incidence angle of 30° the frequency shift of the peak is determined to be 11.46 GHz. As the only parameters of interest are frequency shifts of the modes and their angular dependence, these data are collected and presented in Table 4.5.

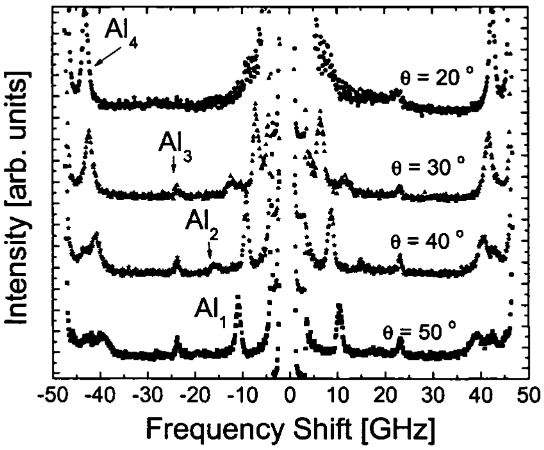

Figure 4.15: Brillouin spectra of the alumina template (T-519) at an *FSR* of 50 *GHz* and with various angles of incidence (as indicated).

The mode of the lowest frequency shift (Al_1) behaves like a surface mode. The plot of frequency shift versus $\sin\theta_i$ is shown in Figure 4.16. It is a straight line of the slope equal to 13.91 GHz. Using the Equation (2.28) the velocity of the surface mode was found to be 3700 $\frac{m}{s}$. The mode observed only in two spectra (Al_2) exhibits the characteristics of a surface mode as well. The slope of the trend line was determined to be 23.4 GHz with an R^2 value of 0.98. This value of the slope would, according to Equation (2.28), give a surface velocity of $\sim$ 6200 m/s. This value of surface phonon velocity is much higher that those of most materials (comparable to surface phonon velocity of hard supported layers [62]). If one assumes that this peak is not due to a surface mode and the frequency shift for $\theta_i = 0$ is not 0 GHz, the line of best fit crosses the frequency shift axis at -1.9 GHz. This value of the intercept is much larger than the estimated uncertainty in frequency shift. This behavior suggests the surface character of the phonon. To figure out the origin of this excitation more data points would be desired. The frequency shift of Al_3 and Al_4 are independent of $\sin\theta_i$. This suggests they may be due to bulk modes.

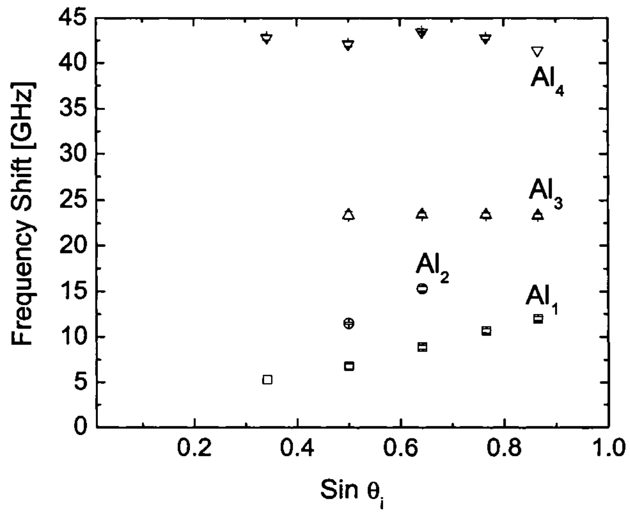

Figure 4.16: The angular dependence of the frequency shifts of $T-519$.

The intensities of the individual peaks are function of the incident angle. The position of the peaks and their intensities vary but under none of the experimental conditions do the spectra resemble those obtained from $CNT-2$ nor are any of the frequency shifts similar. This allows us to make a statement that none of the modes described in Section **4.1.1** is solely due to the alumina substrate.

The values of the frequency shifts of the peaks observed in the spectra collected from $CNT - 0$ (see Table 4.4) are comparable to those presented in Table 4.5. The mode of smaller frequency shift behaves like the surface mode in alumina, the other one can be identified as the mode called Al_4 in spectra collected from $T - 519$ (see Figure 4.16). The latter one is observed in the alumina template with holes with intensity decreasing with the increasing angle of incidence, which may explain why in spectra collected from $CNT - 0$ it can be observed only when θ_i is of 30° and is not present with higher incidence angles. These arguments lead to the conclusion that in our case the peak of the frequency shift of 41.27 GHz observed in spectra collected from $CNT - 0$ can be taken as the mode originating from alumina not from the carbon nanotubes. This allows us to draw the conclusion that both peaks observed in the spectra collected from $CNT - 0$ originate due to the alumina template. The Brillouin spectra collected for $CNT - 0$ in certain regions of frequency resembles those collected from the alumina template $T - 519$, although macroscopically the samples look very different and represent stages of carbon nanotube array production that do not follow each other. The broadening due to the opacity changes the profile of the spectrum and make some peaks invisible, still some characteristics are common.

To finally confirm all of the above conclusions a Brillouin spectrum from an annealed alumina template ($T - 519a$) was collected. Unfortunately no peaks were observed because of a high background.

4.2 Spectra collected with smaller FSR.

The motivation for collecting a spectrum over smaller frequency range was to have a closer look at peaks B_5 and B_7. A Brillouin spectrum collected at an FSR of 12 GHz is presented in Figure 4.17. No new features concerning B_5 and B_7 were noticed. While analyzing this spectrum some additional excitations were observed at a frequency shift of around 1 GHz. Their intensities were significantly larger than the intensities of the peak of initial interest ($5 - 7$ GHz). This is well illustrated in Figure 4.17.

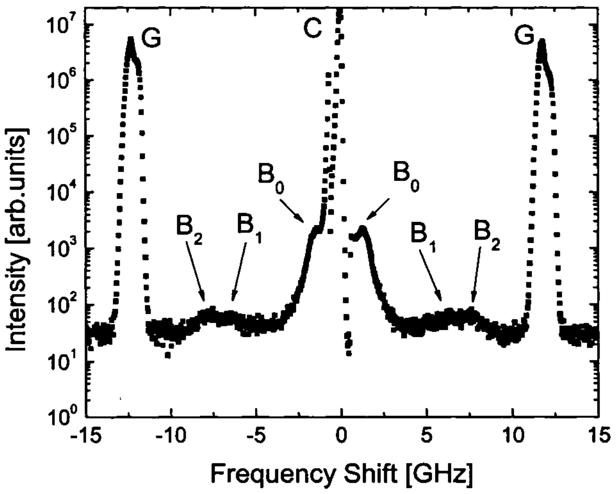

Figure 4.17: A typical spectrum of the $CNT - 2$ at an FSR of 12 GHz in air with a 60° angle of incidence.

In order to study the new peaks more thoroughly, the FSR was decreased to 8

GHz. These spectra were collected with a smaller input pinhole. The chosen size was 200 μm instead of the 450 μm used in the case of the spectra collected at a higher FSR. The advantage of such a choice is that the peak situated close to the elastic peak can be better resolved. A disadvantage is that less light enters the spectrometer and the intensity of the peaks decreases. Therefore peaks B_5 and B_7 are no longer seen in spectra collected at 8 GHz.

4.2.1 Carbon nanotube array with $200-300$ nm of the nanotubes protruding above the alumina surface

Figure 4.18 shows a spectrum collected from $CNT-2$ in vacuum. With the air evacuated from the sample holder the peak labeled B_{OUT} is present. The pressure in the sample holder, initially close to 0 $mmHg$ was found to be $\sim$ 30 $mmHg$ (0.05 atm) at the end of the data collection time ($\sim$ 9 $hours$). The frequency shift, integrated intensity, maximum intensity and width of the peak B_{OUT} are determined assuming the Lorentzian profile of the peak and summarized in Table 4.6. In the Figure 4.18 peak B_{OUT} looks deformed and does not resemble a single Lorentzian curve. Analysis proved that there are two peaks that are present at this region - one at the frequency shift of 1.32 GHz and another around 1.50 GHz (see Figure 4.18, bottom). The latter one was identified as originating from the laser (other longitudinal modes are present in the laser output but at greatly reduced intensity). These peaks appear in most of collected spectra and are very characteristic and easy to recognize - they are

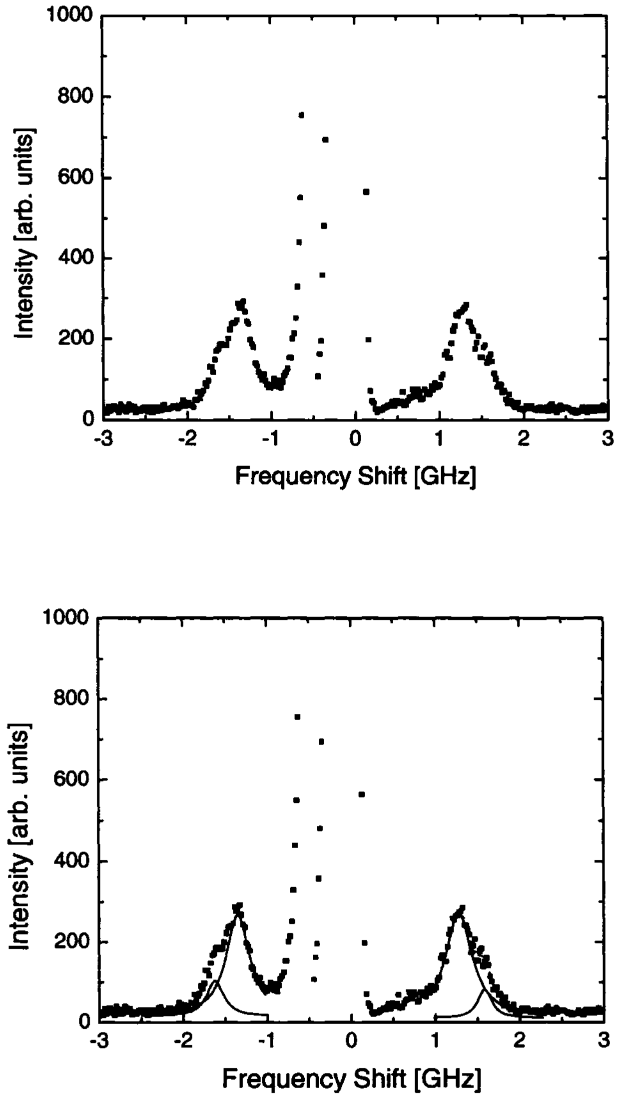

Figure 4.18: Brillouin spectrum of the $CNT - 2$ at an FSR of 8 GHz in vacuum with a 60° angle of incidence (top) and the same spectrum fitted (botttom). Solid lines: individual peaks (B_{OUT}), dotted line: total fit of Lorenzian peaks.

of narrow width, the spacing between them is exactly 0.75 GHz and their intensity decreases exponentially with increasing frequency shift. Although taken into account while analyzing the spectra due to their effect on the shape of the B_{OUT}, they are ignored in further discussion. The presence of the B_{OUT} in the Brillouin spectrum with no presence of the gas in the holder implies that it is due to the nanotube array. To examine these predictions more thoroughly a set of spectra for gases characterized by various masses and polarizabilities (see Table 4.1) forming the nanotube array environment were collected. The order of application of the gases was completely arbitrary and is not followed in the discussion.

A Brillouin spectrum collected in air with this FSR is presented in Figure 4.19 (top spectrum). One set of Brillouin peaks at $\sim$ 1.3 GHz is easily observed. In addition at shifts < 1 GHz there is an increased intensity relative to the background level suggesting the existence of another peak. On the left side the peak labeled B_{OUT} is not distinguished well because of a slight asymmetry in the elastic peak. The frequency shift, integrated intensity, maximum intensity and width of the outer peak B_{OUT} are determined assuming the Lorentzian profile of the peak and summarized in Table 4.6. A peak fitting analysis based on the presence of two peaks resulted in the frequency shift of peak B_{OUT} of 1.19 GHz. The inner peak (labeled by analogy B_{IN}) is determined to be of Gaussian shape (see Figure 4.19, bottom) [42] and its frequency shift is 0 GHz (see Table 4.7). The presence of the inner peak in air (no evidence of it when vacuum surrounded the $CNT-2$) suggests that it originates due

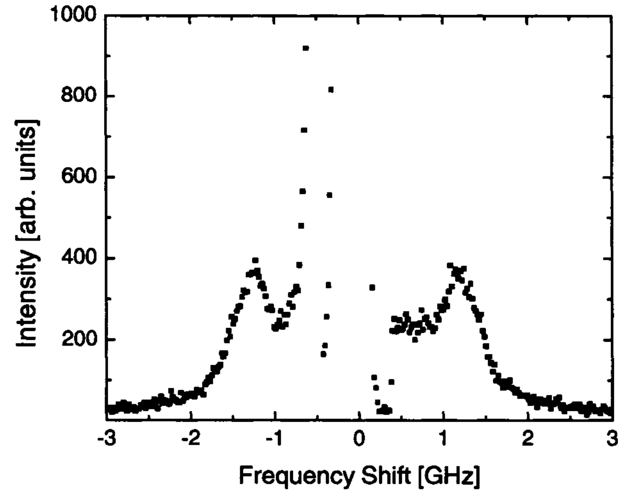

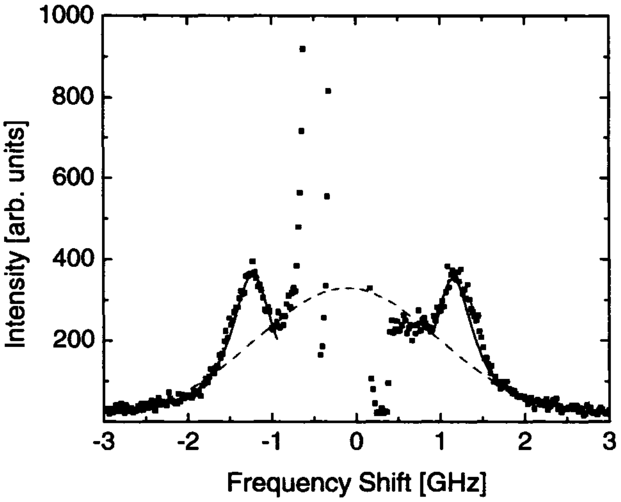

Figure 4.19: The Brillouin spectrum of the $CNT-2$ at an FSR of 8 GHz in air with a 60° angle of incidence not fitted (top) and with fitting lines - dash line: Gaussia (B_{IN}), solid lines: individual peaks (B_{OUT}), dotted line: total fit of Lorenzian peaks (bottom).

to the gas surrounding the nanotubes. In the case of H_2 environment the inner peak B_{IN} is very broad and of low maximum intensity, as shown in Figure 4.20. The low intensity makes a fit impossible. Comparison of the shape of spectra discussed so far ($CNT-2$ in air, vacuum and H_2) makes it evident that in all of them peak B_{OUT} is well defined and of larger maximum intensity than peak B_{IN}. The maximum intensity of the outer peak in hydrogen has significantly changed relative to air and vacuum but the frequency shift is comparable with frequency shifts calculated in these two environments.

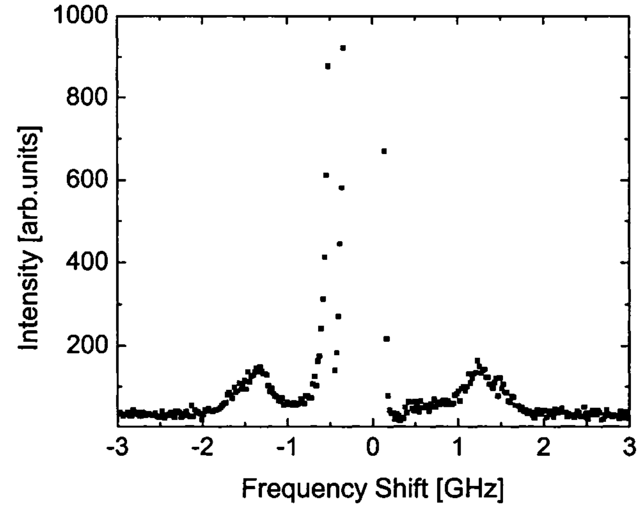

Figure 4.20: Brillouin spectrum of the carbon nanotube array at an FSR of 8 GHz in H_2 with a 60° angle of incidence.

In the case of spectra collected for carbon nanotubes in Ar and CH_4 (Figure 4.21 top and bottom, respectively) the frequency shifts of the outer peaks are com-

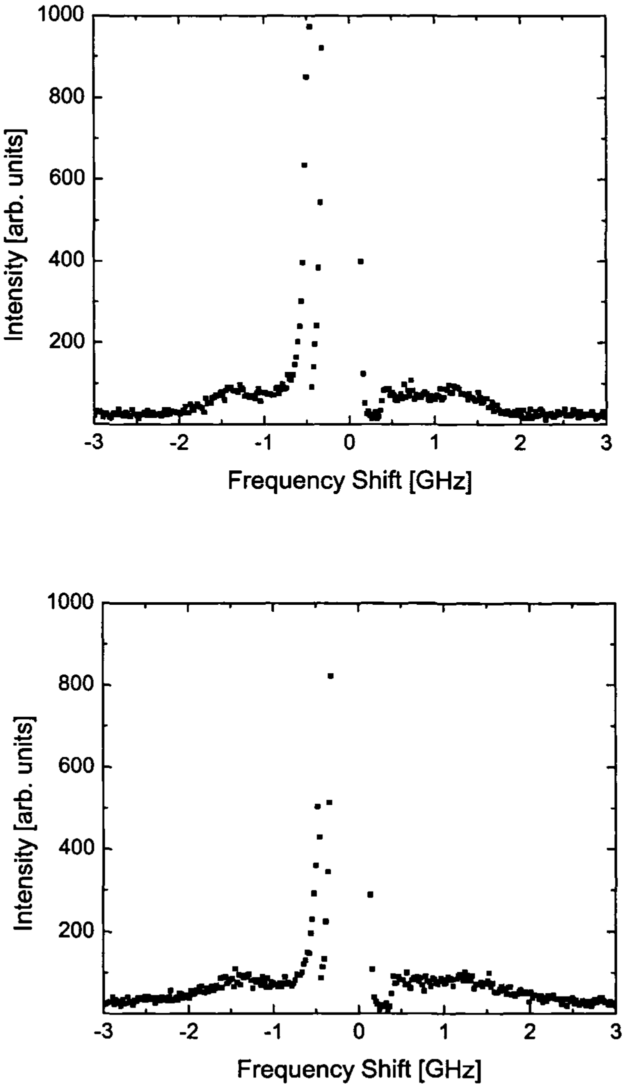

Figure 4.21: Brillouin spectra of the $CNT - 2$ at an FSR of 8 GHz in Ar (top) and CH_4 (bottom) with a 60° angle of incidence.

parable with those calculated and discussed above. The reasons for discussing these two spectra together is that they caused similar problems in fitting analysis. The resolution of the peaks is difficult due to the lack of a well defined border between them, that we can observe for gases discussed earlier. Based on the fit of a single Gaussian peak; the resolution of the B_{OUT} was possible despite the overlapping of the peaks B_{IN} and B_{OUT} and their comparable maximum intensities. The fit for the spectrum of $CNT-2$ in Ar is presented in Figure 4.22. All the parameters (i.e., maximum and integrated intensity, $FWHM$ and frequency shift) evaluated for both peaks are very similar (see Table 4.6) although physical properties of the gases (mass, polarizability, molecular shape [58]) are different.

The frequency shifts of the inner peak B_{IN} in the spectrum of $CNT-2$ in Ar and CH_4 seem to be different from the expected value of 0 GHz. These spectra are also the ones with the highest uncertainty in area of the outer peak. Both these features result from the difference between the Stokes and anti-Stokes region which is caused by the fact that the spectra are not perfectly centered at zero (*i.e.* the elastic peak has an apparent, small. non-zero frequency shift). This systematic imperfection appears in every spectrum and in the cases of Ar and CH_4 it is a few times larger.

When another rare gas, Kr, is used to create the environment inside the sample holder, the B_{IN} peak became more intense than when it was observed in the spectrum of the carbon nanotubes surrounded by Ar (Figure 4.23). Additionally, a significant decrease in its $FWHM$ can be observed (Table 4.7) in comparison with the values

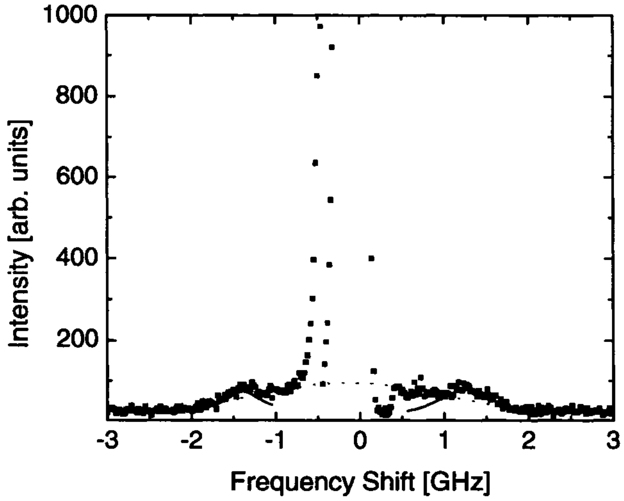

Figure 4.22: Fitted Brillouin spectrum of the $CNT - 2$ in Ar at an FSR of 8 GHz and with a 60° angle of incidence. Dash line - Gaussian line (B_{IN}), solid lines - individual Lorentzian peaks (B_{OUT}).

estimated for lighter gases. The frequency shift of the inner peak is very close to zero.

In CF_4 (Figure 4.24), a gas of methane structure with fluorine atoms substituting the hydrogens, the intensity of the inner peak B_{IN} increases while the width decreases when compared to the spectrum obtained from $CNT - 2$ in CH_4. This observation, along with the differences noticed while comparing spectra collected rom $CNT - 2$ in Ar and Kr, suggests that both intensity of peak B_{IN} and its $FWHM$ depend on the mass of the gas surrounding the $CNT - 2$.

In both cases the outer peak is on the shoulder of the inner one which makes analysis of the less intense one complicated. However the frequency shifts of the outer peak

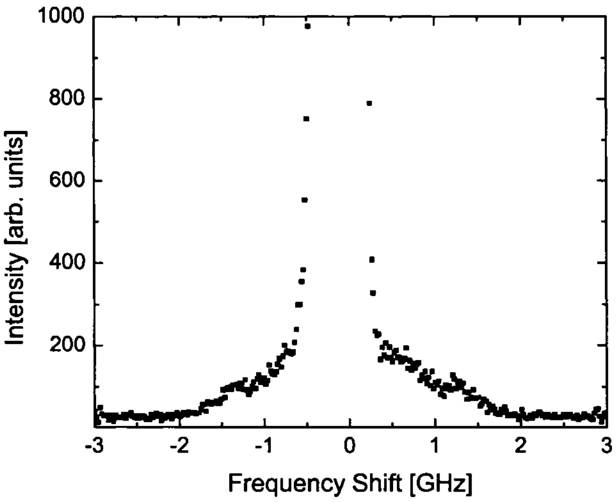

Figure 4.23: Brillouin spectrum of the $CNT-2$ at an FSR of 8 GHz in Kr with a 60° angle of incidence.

B_{OUT} are 1.29 GHz for the nanotube array in Ar and 1.16 GHz when the sample is in CF_4. The latter value is lower than that obtained for gases described before (see Table 4.6) but the uncertainty associated with it allows one to state that it is comparable with all values of the frequency shifts of peak B_{OUT} presented and discussed so far. Despite the similarities there are some unique characteristics observed in each of the two spectra. The maximum intensities and widths of the outer peak B_{OUT} are significantly different which leads to the integrated intensity of the outer peak being a few times larger for the carbon nanotubes in CF_4 while comparing to the spectrum collected when Kr serves as the environment. This could suggest that Kr has a damping effect on the phonon propagating in the investigated sample.

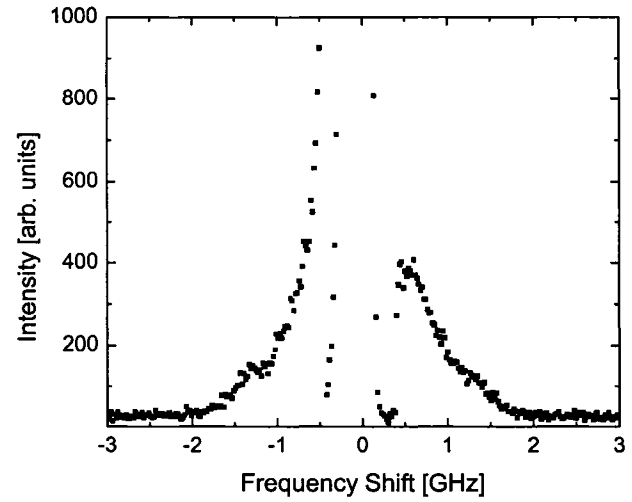

Figure 4.24: Brillouin spectrum of the $CNT-2$ at an FSR of 8 GHz in CF_4 with a 60° angle of incidence.

The trend of increasing intensity of peak B_{IN} continues for substances of more complicated structure and larger mass and polarizability [58] like C_2F_6 and SF_6 (see Figure 4.25). The analysis of the spectra reveals that the $FWHM$ continue to decrease and no changes in the inner peak positions are observed with the increasing molecular mass of the gas.

The integrated intensities, frequency shifts, $FWHM$ and maximum intensities of both B_{OUT} and B_{IN} peaks in each spectrum are summarized and presented in Tables 4.6 and 4.7 respectively. The uncertainty of these values is calculated as the standard deviation for two values. In the case of the inner peak only one value could be read from the spectra. As the correlation coefficient, R^2, for the theoretical Gaussian

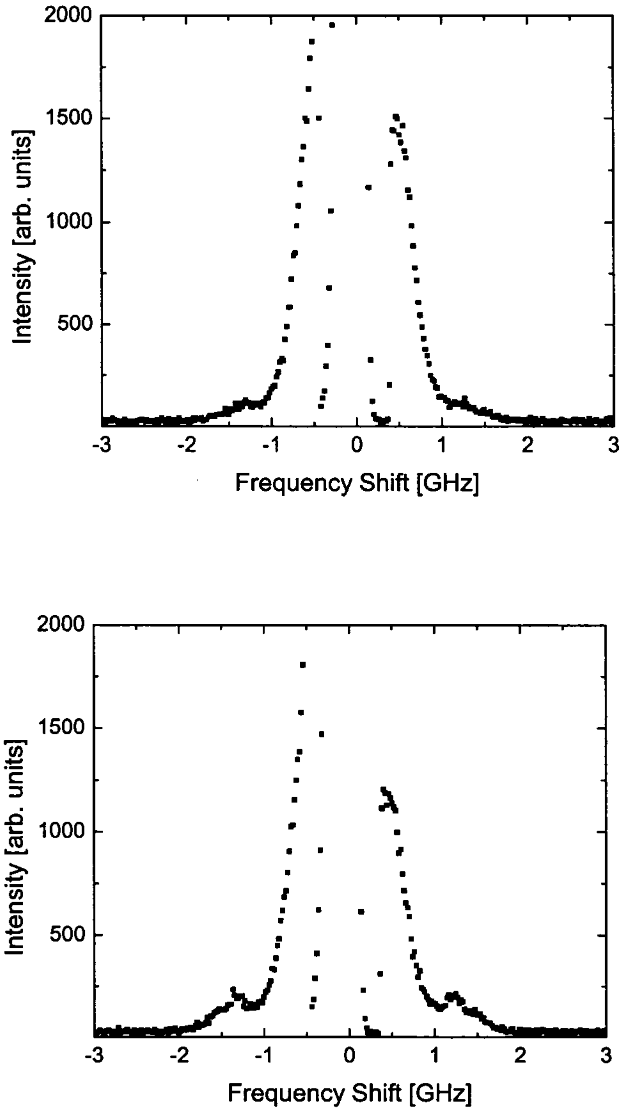

Figure 4.25: Brillouin spectra of the $CNT-2$ at an FSR of 8 GHz in C_2F_6 (top) and SF_6 (bottom) with a 60° angle of incidence.

curve and experimental data, given by software, exceed the value of 0.9, the maximum uncertainty for the data collected for the inner peak is assumed to be about 10%.

Table 4.6: Integrated intensities, frequency shifts, *FWHM* and maximum intensities of the peaks of the B_{OUT} in $CNT-2$

Gas	**Integrated Intensity** [**arb.units** × **GHz**] ×**10^2**]	**Frequency Shift** [**GHz**]	**FWHM** [**GHz**]	**Maximum Intensity** [**arb.units**] ×**10^2**]
Vacuum	1.47 ± 0.12	1.32 ± 0.04	0.36 ± 0.02	2.57 ± 0.04
H_2	0.66 ± 0.06	1.29 ± 0.05	0.37 ± 0.03	1.12 ± 0.02
CH_4	0.83 ± 0.21	1.28 ± 0.08	0.89 ± 0.13	0.59 ± 0.06
Air	3.23 ± 0.11	1.19 ± 0.04	0.60 ± 0.01	3.41 ± 0.05
Ar	0.83 ± 0.14	1.29 ± 0.04	0.76 ± 0.09	0.69 ± 0.04
Kr	0.43 ± 0.05	1.29 ± 0.06	0.40 ± 0.04	0.68 ± 0.01
CF_4	1.89 ± 0.19	1.16 ± 0.11	0.82 ± 0.08	1.45 ± 0.14
C_2F_6	1.07 ± 0.01	1.23 ± 0.04	0.66 ± 0.01	1.02 ± 0.01
SF_6	1.10 ± 0.09	1.26 ± 0.05	0.39 ± 0.04	1.80 ± 0.03

Table 4.7: Integrated intensities, frequency shifts, *FWHM* and maximum intensities of the B_{IN} in $CNT-2$

Gas	**Integrated Intensity** [**arb.units** × **GHz**] ×**10^2**]	**Frequency Shift** [**GHz**]	**FWHM** [**GHz**]	**Maximum Intensity** [**arb.units**] ×**10^2**]
Vacuum	--	--	--	--
H_2	--	--	--	--
CH_4	3.63	−0.05	3.91	0.87
Air	8.76	−0.09	2.60	3.17
Ar	2.16	−0.13	2.62	0.77
Kr	4.34	−0.03	2.15	1.90
CF_4	8.78	−0.02	1.60	5.16
C_2F_6	3.535	−0.02	0.93	35.63
SF_6	27.7	−0.04	0.96	27.02

The changes of intensity are the most significant for the inner peak, B_{IN} as the ratio of the value of maximum intensity I_{IN} in the heaviest gases, C_2F_6 and SF_6, and the value of I_{IN} calculated in hydrogen is of the order of ~ 100. The dependence on the molecular mass of the gas is clear (see Figure 4.26, top), the character of the dependence resembles an exponential function. If the natural logarithm of integrated intensity, I_{IN}, is plotted versus the mass of the gas the trend is approximately linear (presented in Figure 4.26, bottom), with an R^2 value of 0.87. This peak is the one recognized by Young [37] as having a frequency shift of $\sim 0.7\ GHz$. This analysis was based on the assumption that two sets of Brillouin peaks (one at $\sim 0.7\ GHz$ and one at $\sim 1.3\ GHz$) resulting from phonons propagating in the nanotube array are observed. The difference of peak classification arises from the shape of the spectra near the central elastic peak. Both analyses (Lorentzian centered at $\pm 0.7\ GHz$ and single Gaussian centered at $0\ GHz$ for B_{IN}) are acceptable from a statistical point of view. However fitting to a Gaussian consistently gives good fits whereas this is not always the case when a Lorentzian is fitted to the assumed peak at $\pm 0.7\ GHz$. What is more, because of the fact that all spectra are collected in the kinetic regime, the presence of a Gaussian-shaped peak (and not a set of Lorentzian-shaped Brillouin peaks) due to the gas surrounding the carbon nanotube array is expected [63], [64].

The value of integrated intensity obtained for the air does not fall into the trend. The positions of the points and the discrepancy that cannot be ignored suggests more detailed studies of the dependence of the intensity of the light scattered by the gas on its mass, especially from the gases of similar properties (rare gases of higher masses, alkanes). This issue is, however, outside the subject of this thesis.

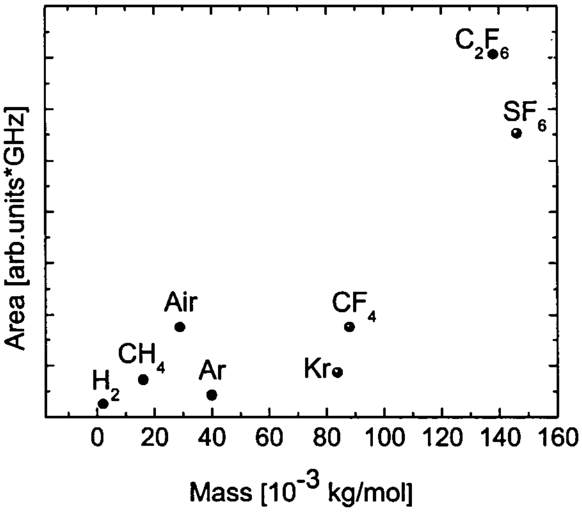

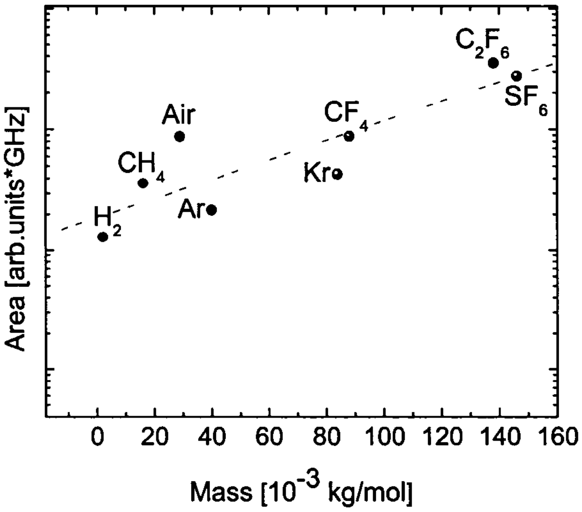

Figure 4.26: Plots of the integrated intensities (top) and of the logarithm of the integrated intensities (bottom) of the inner peak B_{IN} versus the molecular mass of the gas.

The values of $FWHM$ of the inner peak B_{IN} change with the molecular mass of the gas serving as the environment of $CNT-2$. Comparison of the data obtained experimentally with the theoretical values calculated using Equation (2.15) is presented in the Table 4.8 and can be seen in the Figure 4.27. The theoretical and experimental values are comparable within the uncertainty range specified.

Table 4.8: Theoretical and experimental values of $FWHM$ of B_{IN} in various gases.

Gas	**Theoretical values** $[GHz]$	**Experimental values** $[GHz]$
Vacuum	0	−−
H_2	9.73	−−
CH_4	2.94	3.91
Air	2.57	2.60
Ar	2.19	2.63
Kr	1.51	2.15
CF_4	1.47	1.60
C_2F_6	1.18	0.93
SF_6	1.14	0.96

The plot of integrated intensities of peak B_{OUT} versus molecular mass of the gas are presented in Figure 4.28, top. No trend in the behavior of outer peak's intensity with changing mass of the gas surrounding the $CNT-2$ is observed. Inequality of the values of integrated intensity obtained for substances of comparable masses but different polarizability (Ar and CF_4) suggest the sensitivity to the gas polarizability of the outer peak B_{OUT}. No trend can be seen while comparing the integrated intensities of the outer peak B_{OUT} in these and other gases as can be seen in Figure 4.28, bottom. Although the set of data obtained from the analyses vary, the peak B_{OUT} does not

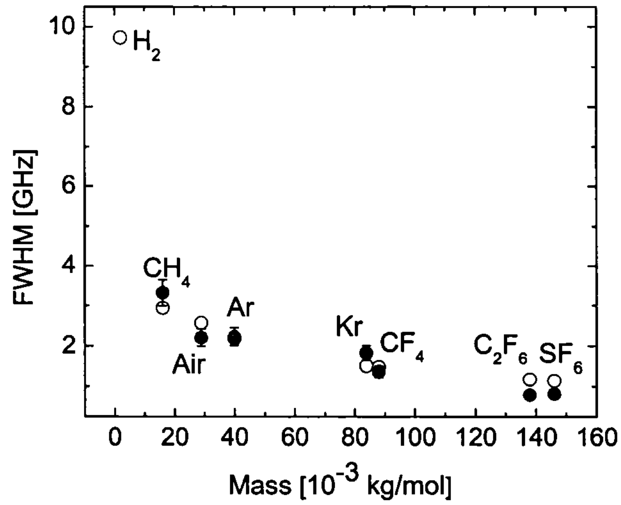

Figure 4.27: Comparison of the plots of the theoretical (open dots) and experimental (solid dots) values of *FWHM* of the inner peak B_{IN} versus the molecular mass of the gas.

seem to trend with mass or polarizability of the gas.

The inner peak is believed to originate from the gas surrounding the carbon nanotube array. A light scattering experiment in a typical gas probes density fluctuations of a wavelength λ comparable to mean free path between collisions, $\bar{l}$ [65]. The Gaussian shape of the spectrum in the region near the center line is characteristic for the gases in the kinetic region ($\bar{l} \ll \lambda$) [63], [64]. The change of the peak's intensity and the *FWHM* are dependent on the gas surrounding the sample. The fact that peak B_{IN} completely disappears in vacuum and the comparison of the spectra of carbon nanotubes in air and of air itself, presented in the Figure 4.29, are arguments

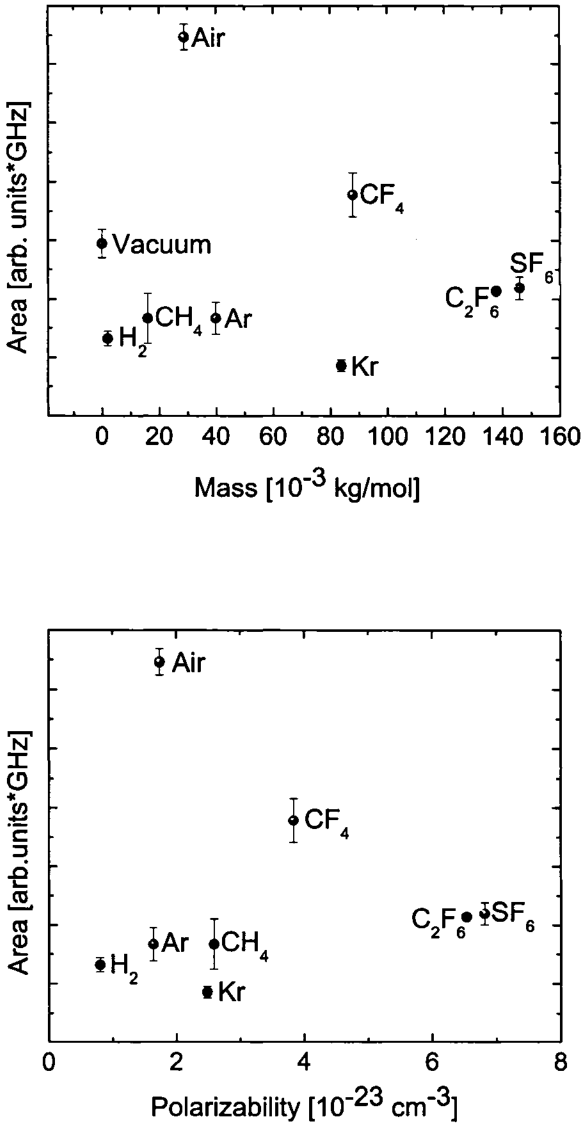

Figure 4.28: Plots of the integrated intensities of the outer peak B_{OUT} versus the molecular mass (top) and polarizability of the gas (bottom).

that support this idea. The spectra overlap in the low frequency region and the shape and frequency shift of the peak of interest are comparable. This proof is not sufficient as the intensity of the peaks at 0 *GHz* is different for each of the spectrum. In order to understand the origin of the peak B_{OUT} and confirm the ideas about the origin of the peak B_{IN} additional data was collected. The carbon nanotube array with 0 *nm* exposed length was examined under the same experimental conditions. The study of this sample, presented below, was neither as complex nor as detailed as the study discussed above.

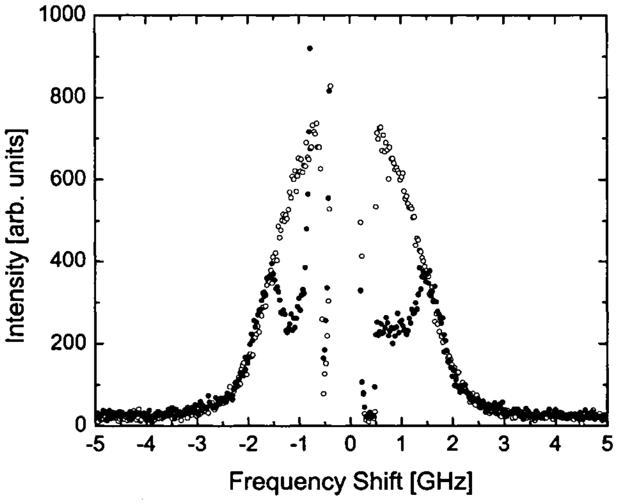

Figure 4.29: Brillouin spectra of carbon nanotubes in air (solid dots) and of air (open dots) at an *FSR* of 8 *GHZ*.

4.2.2 Carbon nanotube array with nanotubes flush with alumina surface

In the region of low frequency the spectra of $CNT-0$ in vacuum and in air were collected. A comparison of the Brillouin spectra collected from $CNT-2$ and $CNT-0$ under the same experimental conditions from is presented in the Figure 4.30. No peaks are observed in this frequency range in spectra collected from $CNT-0$ in vacuum. The comparison of Brillouin spectra of $CNT-0$ and $CNT-2$ in vacuum presented in Figure 4.30 also shows that the peak at $\sim 1.3\ GHz$ is observed only in the $CNT-2$ spectra (*i.e.* in the nanotube array in which the nanotubes protrude above the top surface of the alumina template by $200-300\ nm$).

When the spectrum of $CNT-0$ in air was collected it turned out that the only peak observed in this spectrum is the Gaussian peak originating from the air surrounding the $CNT-0$ sample. In this case the comparison of spectra collected from $CNT-0$ and $CNT-2$ (see Figure 4.30, bottom) shows that the only common part of both of them is the Gaussian peak originating due to light scattering from the gas surrounding the sample. The intensities and shapes of the lines are exactly the same for both spectra. Apart from this peak no additional modes from the unexposed nanotubes have been observed at low frequency range in presence of the gas. The absence of the peak at a frequency shift of $\sim 1.3\ GHz$ that was observed in $CNT-2$ confirms the prediction that it originates from the exposed length of the nanotubes

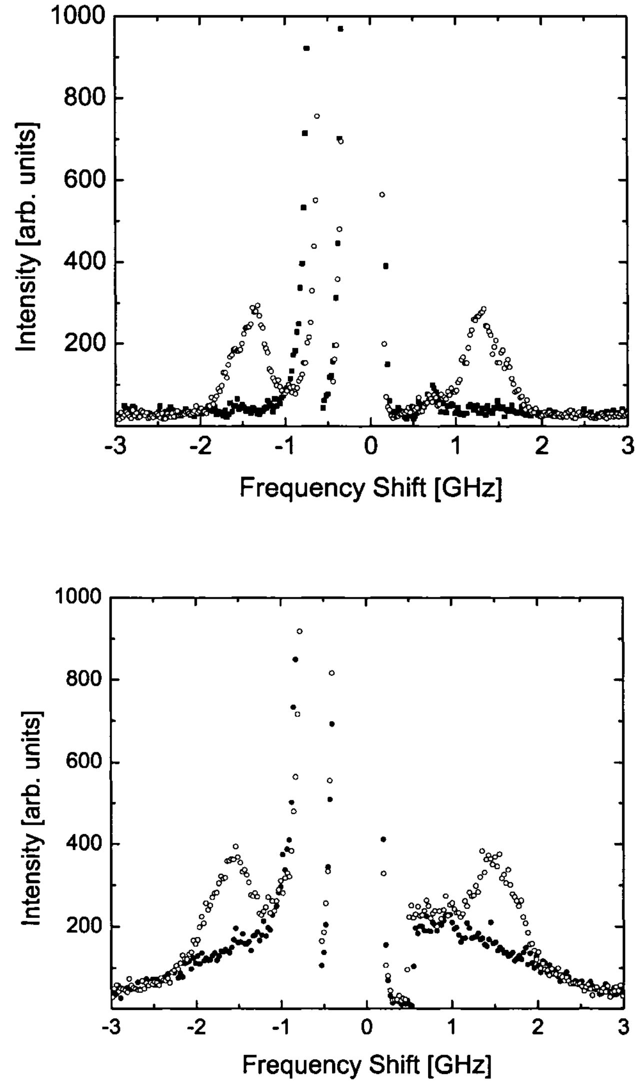

Figure 4.30: Brillouin spectra of the $CNT-2$ (open dots) and $CNT-0$ (solid dots) in the low-frequency range in vacuum (top) and in air(bottom).

comprising the array. As mentioned above, its presence and frequency shift does not depend on the gas surrounding the sample and the peak is present even in vacuum. This suggests that the phonon could either originate due to the array when coupling via the alumina substrate occurs or could be the transverse, longitudinal or twist (torsional) mode [66] that propagates in the individual nanotubes.

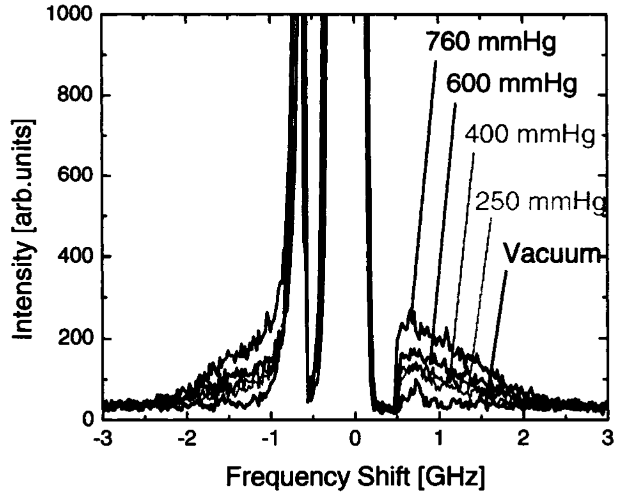

Figure 4.31: The Brillouin spectra of $CNT - 0$ at various pressure of the air surrounding the sample.

To finally confirm the origin of the peak B_{IN}, spectra from $CNT - 0$ at an FSR of 8 GHz were collected in air at various pressures from vacuum up to 1 atm (see Figure 4.31). The intensity of the Gaussian peak changes when the pressure of the air surrounding the sample is changed. This study provides confirmation that the peak at a frequency shift of 0 GHz originates from the gas surrounding the sample and is of Gaussian shape. The integrated intensities, frequency shifts, $FWHM$ and maximum intensities of the peak in the air at different the values of the pressure are summarized in Table 4.9. The data confirm that value of the integrated intensity increases as the pressure of the gas increases.

Table 4.9: Integrated intensities, frequency shifts, $FWHM$ and maximum intensities of the peak originating due to the air surrounding the $CNT-0$.

Pressure $[mmHg]$	**Integrated Intensity** $[arb.units * GHz]$	**Frequency Shift** $[GHz]$	**FWHM** $[GHz]$	**Maximum Intensity** $[arb.units]$
760	767	−0.07	2.18	281
600	486	−0.06	2.20	176
400	360	−0.06	2.22	129
250	284	−0.08	1.88	121
0	−−	−−	−−	−−

4.3 Determination of phonon velocities

If one treats the structures of the nanotubes and graphite as similar enough to apply the same refractive index to both media and assumes that the carbon nanotube array can be treated as a porous material, the velocities of bulk modes observed in $CNT-2$ may be calculated. It should be clearly stated that the obtained values are only estimates due to these assumptions.

Using the refractive index of graphite to be 2.15 [67] and estimating from the Figure 3.6 that the upper limit of the percentage volume of the space occupied by protruding nanotubes in $CNT-2$ is 15%, the refractive index n of the $CNT-2$ in this region is determined using an effective medium approximation [68] to be 1.71.

From Equation (2.13) the velocity of the each mode was determined. The velocity of the mode at $\sim 1.3\ GHz$ frequency shift were of the order of a few hundreds of meters per second. This value is quite low - in fact this is comparable to the speed of sound in air. The velocities of modes B_5 and B_7 depended on the gaseous environment around the sample and varied from 1000 to 2000 $\frac{m}{s}$, which is of the order of the speed of sound in solids. The obtained values were calculated with the assumption that observed phonons are propagating through the array - possibly via coupling of the tube vibration through the substrate or interactions between the protruding length of the tubes. However, observed modes may also be transverse, longitudinal or torsional modes that propagate in individual tubes. At this point the origin of the peaks cannot be definitely determined.

The determination of the elastic moduli of the array require an estimate of its density. This approximation, coupled with the already made estimate of the phonon velocities, would, however not result in meaningful values.

Chapter 5

Conclusion

Brillouin spectra were collected from four samples representing various stages of fabrication of carbon nanotube arrays. These are: (i) anodized alumina template with holes arranged in close-packed hexagonal array, (ii) annealed alumina template with holes, (iii) carbon nanotube array with nanotubes flush with the surface of alumina substrate and (iv) carbon nanotube array with $200-300\ nm$ of tubes protruding above the surface. Samples were exposed to various gases and vacuum in order to observe peaks and determine and/or confirm their origin.

A Gaussian peak (B_{IN}) originating from the gas surrounding the nanotubes was observed. The increase in the intensity of the peak with increasing pressure, exponential dependence of the intensity of the peak on the mass of the gas, and the agreement of experimental values of $FWHM$ with theoretical calculations confirms the origin of this peak.

A peak at a frequency shift of $\sim 1.3\ GHz$ (B_{OUT}) is present in spectra collected from $CNT-2$ even in the absence of gas (*i.e.*, under vacuum). This suggests that the phonon propagates either in the individual nanotubes or coupling via the alumina substrate occurs.

The intensities and frequency shifts of the peaks at 5 (B_5) and 7 GHz (B_7) are dependent on the gas surrounding the nanotubes. This suggests that the elastic properties of carbon nanotubes may be affected by the presence of a gas. What is more, the qualitative difference in the spectra of $CNT-2$ in H_2 shows that H_2 interacts uniquely with carbon nanotubes.

None of the peaks seen in the spectra of $CNT-2$ are observed in the spectra collected from $T-519$, $T-519a$ and $CNT-0$. From this fact one can conclude that the peaks observed in the $CNT-2$ spectra are due to the length of the nanotubes protruding above the alumina surface. All of the modes exhibit characteristics of bulk modes. It cannot be determined whether the observed phonons propagate through the array (possibly via coupling of tube vibration through the substrate) or if they are transverse, longitudinal or twist (torsional) modes [66] that propagate in the individual tubes. In the first case the values of phonon velocities were estimated using a coarse approximation. They were found to be a few hundreds meters per second for the peak at $\sim 1.3\ GHz$ and between $1000-2000\ \frac{m}{s}$ for peaks at 5 and 7 GHz, depending on the gas surrounding the $CNT-2$ sample.

The aim of future work is to determine the character of the modes and to calculate the elastic moduli of the array. The first step to achieve this goal may be to investigate the samples representing other stages of the fabrication of carbon nanotube arrays (*i.e.*, other than those discussed in this thesis). This might include carbon nanotube array samples with shorter protruding lengths (*e.g.*, 100 *nm*) as well as longer values. The latter one could be particularly interesting as after exceeding a length of ~ 300 *nm* the protruding nanotubes start to bend and create a "the haystack" structure. Future work may include extended research on the elastic properties of the nanotube arrays in the presence of various gaseous environments (*e.g.*, rare gases, gases belong to alkane group, toxic gases). This could aid in the understanding of the interactions between gases and nanotubes as well as to determine possible applications, especially those regarding the use of carbon nanotube arrays in gas sensors.

Bibliography

[1] F. Kreupl, A.P. Graham, G.S. Duesberg, W. Steinhögl, M. Liebau, E. Unger, and W. Hönlein. *Microelectron. Eng.*, 64:399–408, 2002.

[2] S. Iijma. *Nature*, 354:56–58, November 1991.

[3] N. Hamada, S. Sawada, and A. Oshiyama. *Phys. Rev. Lett.*, 68(10):1579 – 1581, 1992.

[4] M. Baxendale. *J. Mater. Sci.-Mater. El.*, 14:657–659, 2003.

[5] R.H. Baughman, A.A. Zakhidow, and W.A. de Heer. *Science*, 297:787–792, August 2002.

[6] J.P. Lu. *Phys. Rev. Lett.*, 79(7):1297–1300, August 1997.

[7] J. Che, T. Çağin, and W.A. Goddard. *Nanotechnology*, 11:65–69, 2000.

[8] V.N. Popov. *Mater Sci. Eng.*, R 43:61–102, 2004.

[9] A. Goldoni, R. Larciprete, L. Peteccia, and S. Lizzit. *J. Am. Chem. Soc.*, 125:11329–11333, August 2003.

[10] S.J. Tans, A.R.M. Verschueren, and C. Dekker. *Nature*, 393:49–52, May 1998.

[11] R.Martel, T. Schmidt, H.R. Shea, T. Hertel, and Ph. Avouris. *Appl. Phys. Lett.*, 73(17):2447–2449, October 1998.

[12] H.W. Ch. Postma, T. Teepen, Z. Yao, M. Grifoni, and C. Dekker. *Science*, 293:76–79, July 2001.

[13] A.G. Rinzler, J.H. Hafner, P. Nikolaev, L. Lou, S.G. Kim, D. Tománek, and P. Nordlander amd D.T. Colbert and. R.E. Smalley. *Science*, 269:1550–1553, September 1995.

[14] A. Bachtold, P. Hadley, T. Nakanishi, and C. Dekker. *Science*, 294:1317–1318, November 2001.

[15] M.R. Pederson and J.Q. Broughton. *Phys. Rev. Lett.*, 69(18):2689–2692, 1992.

[16] S. Niyogi and R.C. Haddon. *PNAS*, 101(17):6331–6332, 2004.

[17] J. Kong, N.R. Franklin, C. Zhou, M.G. Chapline, S. Peng, K. Cho, and H. Dai. *Science*, 287:622–625, 2000.

[18] M. Ishigami A. Zettl P.G. Collins, K. Bradley. *Science*, 287:1801–1804, March 2000.

[19] S. Jhi, S. Louie, and M. Cohen. *Phys. Rev. Lett.*, 85(8):1710–1713, 2000.

[20] P. Giannozzi, R. Car, and G. Scoles. *J. Chem. Phys*, 118(3):1003–1006, 2003.

[21] H. Ulbricht, G. Moos, and T. Hertel. *Phys. Rev. B*, 66(075404), August 2002.

[22] G.U. Sumanasekera, C.K.W. Adu, S. Fang, and P.C. Eklund. *Phys. Rev. Lett.*, 85(5):1096–1099, July 2000.

[23] A.C. Dillon, K.M. Jones, T.A. Bekkedahl, C.H. Kiabg, D.S. Bethune, and M.J. Heben. *Nature*, 386:377–379, March 1997.

[24] A. Chambers, C. Park, R. Terry, and K. Barker amd N. M. Rodriguez. *J. Phys. Chem. B*, 102(22):4253–4256, 1998.

[25] G. Che, B.B. Lakshmi, E.R. Fisher, and C.R. Martin. *Nature*, 393:346–349, 1998.

[26] K. Sato, M. Noguch, A. Demach, N. Oki, and M. Endo. *Science*, 264:556–561, 1994.

[27] R.J. Tonucci, B.L. Justus, A.J. Campillo, and C.E. Ford. *Science*, 258:783, 1992.

[28] J.M. Xu. *Infrared Phys. Techn.*, 42:485–491, 2001.

[29] S.K. Biswas, R. Vajtai, B. Wei, G. Meng, L.J. Schwalter, and P.M. Ajayan. *Appl. Phys. Lett.*, 84(15):2889-2891, 2004.

[30] S.S. Xie, W.Z. Li, Z.W. Pan, B.H. Chang, and L.F. Sun. *Eur. Phys. J. D*, 9:85–89, 1999.

[31] D. Kim, D. Cho, H. Jang, C. Kim, and H. Lee. *Nanotechnology*, 14:1269–1271, 2003.

[32] J. Li, C. Papadopoulus, and J.M. Xu. *Appl. Phys. Lett.*, 75(3):367–369, May 1999.

[33] J.S. Suh and J.S. Lee. *Appl. Phys. Lett.*, 75(14):2047–2049, 1999.

[34] C.E. Bottani, A.Li Bassi, M.G. Beghi, A. Podestà, P. Milani, A. Zakhidov, R. Baughman, D.A. Walters, and R.E. Smalley. *Phys. Rev. B*, 67(155407), April 2003.

[35] A. Li Bassi, M.G. Beghi, C.S. Casari, C.E. Bottani, A. Podestà, P. Milani, A. Zakhidov, R. Baughman, D.A. Walters, and R.E. Smalley. *Diam. Relat. Mater.*, 12:806–810, 2003.

[36] A. Li Bassi, C.E. Bottani, C. Casari, and M. Beghi. *Appl. Surf. Sci.*, 226:271–281, 2004.

[37] C.K. Young. *Brillouin Scattering From Carbon Nanotube Arrays - Honours Thesis.* St. John's, June 2004.

[38] P. Murugavel, C. Naraywana, A. Govindraj, A.K. Sood, and C.N.R. Rao. *Chem Phys Lett*, 331:149–153, 2000.

[39] R.S. Krishnan. *The Raman Effect*, volume 1, chapter Brillouin Scattering, pages 343–402. Marcel Dekker INC., New York, 1971.

[40] Ch. Kittel. *Wstęp do fizyki ciała stałego.* Wydawnictwo Naukowe PWN, Warszawa, 1999.

[41] I.L. Fabelinskii. *Molecular Scattering of Light.* Plenum Press, New York, 1968.

[42] A.D. May, E.G. Rawson, and H.L. Welsh.

[43] R. Loudon and J.R. Sandercock. *J.Phys. C: Solid St. Phys.*, 13:2609–2622, 1980.

[44] E. Hecht. *Optics.* Addison Wesley, San Francisco, 4th edition, 2002.

[45] P.R. Stoddart, J.C. Crowhurst, A.G. Every, and J.D. Comins. *J. Opt. Soc. Am. B*, 15(9):2481–2489, September 1998.

[46] F. Nizzoli. *Electromagnetic Surface Excitations*, chapter Surface Brillouin and Raman Scattering, pages 138–161. Springer-Verlag, 1986.

[47] J.R. Sandercock. *Solid State Commun.*, 26:547–551, 1978.

[48] A. Dervisch and R. Loudon. *J. Phys. C: Solid State Phys.*, 9:L669–L673, 1976.

[49] N.L. Rowell and G.I. Stegman. *Phys. Rev. B*, 18(6):2598–2615, 1978.

[50] R. Loudon. *J. Phys.C: Solid State Phys.*, 11:403–417, 1978.

[51] J.D. Comins, A.G. Every, P.R. Stoddart, X. Zhang, J.C. Crowhurst, and G.R. Hearne. *Ultrasonics*, 38:450–458, 2000.

[52] S. Mielcarek. *Spektroskopia Brillouin fononòw powierzchniowych w kryształach ferroelastycznych.* Wydawnictwo Naukowe UAM, 2001.

[53] B.E.A. Saleh and M.C. Tech. *Fundamentals of photonics.* Wiley Interscience Publication, New York, 1991.

[54] J.R. Sandercock. *Light Scattering in Solids*, volume III, chapter Trends in Brillouin Scattering: Studies of Opaque Materials, Supported Films and Central Modes. Springer-Verlag, 1982.

[55] J.R. Sandercock. *Tandem Fabry-Perot Interferometer TFP-1.* Fabrik am Weiher, CH-8909 Zwillikon, Switzerland.

[56] R.H. Petrucci and W.S. Harwood. *General Chemistry - Principles and Modern Application.* Maxwell MacMillan Canada, Toronto, 6th edition, 1993.

[57] N.W. Ashcroft and N.D. Mermin. *Solid State Physics.* Brooks/Cole Thomson Learning, Toronto, 1976.

[58] R.C. Weast and M.J. Astle, editors. *CRC Handbook of Chemistry and Physics.* CRC Press, Inc., Boca Raton, 60th edition, 1979.

[59] Y.M. Sirenko, M.A. Strocio, and K.W. Kim. *Phys. Rev. E*, 53(1):1003–1010, January 1996.

[60] D. Kand, K.W. Kim, and M.A. Stroscio. *J. Appl. Phys.*, 89(9), 2001.

[61] J. Bernholc, D. Brenner, M. Buongiorno Nardeli, V. Meunier, and C. Roland. *Annu. Rev. Mater. Res.*, 32:347–375, 2002.

[62] M. Chirita, R. Sooryakumar, and H. Xia. *Phys. Rev. B*, 60(8):R5153–R5156, 1999.

[63] V. Ghaem-Maghami and A.D. May. *Phys. Rev. A*, 22(2):692–697, 1980.

[64] R.D. Mountain. *Rev. Mod. Phys.*, 38(1):205–214, 1966.

[65] N.A. Clark. *Phys. Rev. A*, 12(1):232–244, 1975.

[66] Y. Xialo, X.H. Yan, J.X. Cao, and J.W. Ding. *J. Phys. Condens. Matter*, 15:L341–L347, 2003.

[67] B.T. Kelly. *Physics of Graphite.* Applied Science Publishers, London, 1981.

[68] H.J. Fan, M.H. Kuok, S.C. Ng, R. Boukherroub, J.-M. Barribeau, J.W. Fraser, and D.J. Lockwood. *Phys. Rev. B*, 65:165330, 2002.